The Astrophysical Journal, 891:120 (25pp), 2020 March 10 https://doi.org/10.3847/1538-4357/ab7455
© 2020. The American Astronomical Society. All rights reserved.

The Nature of γ-Ray Variability in Blazars

Gopal Bhatta[1] and Niraj Dhital[2]
[1] Astronomical Observatory of the Jagiellonian University, ul. Orla 171, 30-244 Kraków, Poland; gopal@oa.uj.edu.pl
[2] Institute of Nuclear Physics PAN, Radzikowskiego 152, 31-342, Kraków, Poland
Received 2019 November 18; revised 2020 January 29; accepted 2020 February 7; published 2020 March 12

Abstract

We present an in-depth and systematic variability study of a sample of 20 powerful blazars, including 12 BL Lacs and 8 flat-spectrum radio quasars, applying various analysis tools such as flux distribution, symmetry analysis, and time-series analysis on the decade-long *Fermi*/LAT observations. The results show that blazars with steeper γ-ray spectral indexes are found to be more variable, and the γ-ray flux distribution closely resembles a log-normal probability distribution function. The statistical variability properties of the sources as studied by power spectral density analysis are consistent with *flicker noise* ($P(\nu) \propto 1/\nu$)—an indication of long-memory processes at work. Statistical analysis of the distribution of flux rise and decay rates in the light curves of the sources, aimed at distinguishing between particle acceleration and energy-dissipation timescales, counterintuitively suggests that both kinds of rates follow a similar distribution and the derived mean variability timescales are on the order of a few weeks. The corresponding emission region size is used to constrain the location of γ-ray production sites in the sources to be a few parsecs. Additionally, using Lomb–Scargle periodogram and weighted wavelet z-transform methods and extensive Monte Carlo simulations, we detected year-timescale quasi-periodic oscillations in the sources S5 0716+714, Mrk 421, ON +325, PKS 1424−418, and PKS 2155−304. The detection significance was computed taking proper account of the red noise and other artifacts inherent in the observations. We explain the results in light of current blazar models with relativistic shocks propagating down the jet viewed close to the line of sight.

Unified Astronomy Thesaurus concepts: High energy astrophysics (739); Blazars (164); Relativistic jets (1390)

1. Introduction

Active galactic nuclei (AGNs) are the most luminous sources ($L \sim 10^{47}$ erg s^{-1}) with supermassive black holes lurking at their centers (see Event Horizon Telescope Collaboration et al. 2019, for M87 galaxy black hole). The sources are powered by accretion onto the supermassive black holes. A small fraction of AGNs (∼10%) profusely emit in radio frequency and, thereby, are known as radio-loud sources. A sub-population of radio-loud AGNs that eject relativistic jets toward us are known as blazars. The sources are known to possess extreme properties such as high luminosity, rapid flux, and polarization variability. Also, blazars are the sources of the abundant nonthermal emission that is Doppler boosted due to the relativistic effects, which makes them appear highly variable over a wide range of spatial and temporal frequencies. Besides, the objects could be sources of extra-solar neutrinos (see IceCube Collaboration et al. 2018a, 2018b). The spectral energy distribution (SED) of the broadband continuum emission from the sources is usually characterized by two distinct spectral peaks. The low-energy peak, which usually lies between the radio and the X-ray energies, is attributed to the synchrotron emission from the relativistic particles, whereas the high-energy peak, usually observed between the UV and the γ-ray energies, is believed to originate from inverse-Compton scattering of low-energy photons (for recent blazar overview, see Böttcher 2019, and references therein). However, there is no common agreement on the source of these low-energy seed photons. Of the two widely discussed models, the synchrotron self-Compton (SSC) model (e.g., Maraschi et al. 1992; Mastichiadis & Kirk 2002) assumes that the same population of electrons emitting synchrotron photons up-scatters these photons to higher energies, whereas the external Compton (EC) model assumes that the softer seed photons are provided by various regions of AGNs, such as an accretion disk (AD; Dermer & Schlickeiser 1993), broad-line region (BLR; Sikora 1994), and dusty torus (DT; Błażejowski et al. 2000).

Based on the presence of the emission lines over the continuum in their SEDs, blazars are grouped into two subclasses: more luminous flat-spectrum radio quasars (FSRQ), which show emission lines over the continuum, and less powerful BL Lacertae (BL Lac) sources, which show weak or no such lines. In the case of FSRQs, the synchrotron peak is in the lower frequency, and the most plausible process responsible for the high-energy emission is believed to be EC as opposed to SSC (Ghisellini et al. 1998). This is because the sources are known to have abundant seed photons from AD, BLR, and DT (Ghisellini et al. 2011). In the case of BL Lac objects, the synchrotron peak lies in the optical or X-ray regions. These constitute an extreme class of sources featuring high-energy emission from a few tens of keV to TeV energies that results from the combination of the synchrotron and IC processes. The absence of strong circumnuclear photon fields and relatively low accretion rates could be the possible reasons behind the apparent low luminosity for such sources. Another scheme for blazar classification is based on the frequency of the synchrotron peak (ν_s), following which blazars are either high synchrotron peaked blazars (HSP; $\nu_s > 10^{15}$ Hz), intermediate synchrotron peaked blazars (ISP; $10^{14} < \nu_s < 10^{15}$ Hz), or low synchrotron peaked blazars (LSP; $\nu_s < 10^{14}$ Hz; Abdo et al. 2010b; see Fan et al. 2016 for similar recent classification scheme). In the blazar sequence (a scheme to unify the diverse appearance of the sources), bolometric luminosity is found to decrease along with the γ-ray emission in the direction from FSRQ to HSP, but the peak frequencies move toward higher energies (Fossati et al. 1998; Ghisellini et al. 2017). Also, while

Table 1
Source Sample of the *Fermi*/LAT Blazars

Source Name (1)	3FGL Name (2)	Source Class (3)	R.A. (J2000) (4)	Decl. (J2000) (5)	Redshift (6)	FV (%) (7)	$\beta \pm \Delta\beta$ (8)
3C 66A	3FGL J0222.6+4301	BL Lac	$02^h22^m41\overset{s}{.}6$	$+43^d02^m35\overset{s}{.}5$	0.444	58.43 ± 1.78	0.90 ± 0.17
AO 0235+164	3FGL J0238.6+1636	BL Lac	$02^h38^m38\overset{s}{.}9$	$+16^d36^m59^s$	0.94	95.53 ± 1.12	1.40 ± 0.19
PKS 0454−234	3FGLJ0457.0-2324	BL Lac	$04^h57^m03\overset{s}{.}2$	$-23^d24^m52^s$	1.003	68.25 ± 1.06	1.10 ± 0.09
S5 0716+714	3FGL J0721.9+7120	BL Lac	$07^h21^m53\overset{s}{.}4$	$+71^d20^m36^s$	0.3	62.20 ± 1.05	1.00 ± 0.15
Mrk 421	3FGLJ1104.4+3812	BL Lac	$11^h04^m273^s$	$+38^d12^m32^s$	0.03	43.65 ± 1.45	1.00 ± 0.08
TON 0599	3FGL J1159.5+2914	BL Lac	$11^h59^m31\overset{s}{.}8$	$+29^d14^m44^s$	0.7247	111.69 ± 0.88	1.30 ± 0.15
ON +325	3FGL J1217.8+3007	BL Lac	$12^h17^m52\overset{s}{.}1$	$+30^d07^m01^s$	0.131	43.78 ± 4.60	0.80 ± 0.14
W Comae	3FGL J1221.4+2814	BL Lac	$12^h21^m31\overset{s}{.}7$	$+28^d13^m59^s$	0.102	24.70 ± 8.87	1.10 ± 0.09
4C +21.35	3FGLJ1224.9+2122	FSRQ	$12^h24^m54\overset{s}{.}4$	$+21^d22^m46^s$	0.432	114.91 ± 0.59	1.10 ± 0.12
3C 273	3FGL J1229.1+0202	FSRQ	$12^h29^m06\overset{s}{.}6997$	$+02^d03^m08\overset{s}{.}598$	0.158	94.66 ± 0.98	1.20 ± 0.17
3C 279	3FGL J1256.1-0547	FSRQ	$12^h56^m11\overset{s}{.}1665$	$-05^d47^m21\overset{s}{.}523$	0.536	104.29 ± 0.46	1.10 ± 0.16
PKS 1424−418	3FGLJ1427.9-4206	FSRQ	$14^h27^m56\overset{s}{.}3$	$-42^d06^m19^s$	1.522	70.44 ± 0.69	1.5 ± 0.13
PKS 1502+106	3FGLJ1504.4+1029	FSRQ	$15^h04^m25^s.0$	$+10^d29^m39^s$	1.84	90.11 ± 0.70	1.3 ± 0.10
4C+38.41	3FGL J1635.2+3809	FSRQ	$16^h35^m15\overset{s}{.}5$	$+38^d08^m04^s$	1.813	92.99 ± 0.72	1.2 ± 0.15
Mrk 501	3FGL J1653.9+3945	BL Lac	$16^h53^m52\overset{s}{.}2167$	$+39^d45^m36\overset{s}{.}609$	0.0334	33.47 ± 3.76	1.10 ± 10
1ES 1959+65	3FGL J2000.0+6509	BL Lac	$19^h59^m59\overset{s}{.}8521$	$+65^d08^m54\overset{s}{.}652$	0.048	49.55 ± 2.84	1.10 ± 0.14
PKS 2155−304	3FGL J2158.8-3013	BL Lac	$21^h58^m52\overset{s}{.}0651$	$-30^d13^m32\overset{s}{.}118$	0.116	45.93 ± 2.02	0.90 ± 0.20
BL Lac	3FGL J2202.7+4217	BL Lac	$22^h02^m43\overset{s}{.}3$	$+42^d16^m40^s$	0.068	64.10 ± 1.05	1.0±0.10
CTA 102	3FGL J2232.5+1143	FSRQ	$22^h32^m36\overset{s}{.}4$	$+11^d43^m51^s$	1.037	117.42 ± 0.37	1.20 ± 0.19
3C 454.3	3FGL J2254.0+1608	FSRQ	$22^h53^m57\overset{s}{.}7$	$+16^d08^m54^s$	0.859	81.30 ± 0.30	1.30±0.17

synchrotron and γ-ray emission are comparable in HSP sources, FSRQs are mostly γ-ray (or Compton) dominant.

Blazars exhibit variability across the electromagnetic spectrum on diverse timescales that span a few minutes to a few decades. For this reason, multifrequency variability studies could be one of the most relevant tools that can offer important insights into the physical conditions prevailing the innermost regions of blazar jets, including the nature of the dominant particle acceleration and energy-dissipation mechanism, magnetic field geometry, jet content, etc. There have been numerous attempts to model the phenomenon by relating the sources of the variability to a wide range of possible physical processes occurring either in the accretion disk and/or in the jet; the various scenarios include emission sites at the accretion disk revolving around the supermassive black hole, various magnetohydrodynamic instabilities in the disk and the jets, shocks traveling down the turbulent jets, and relativistic effects due to jet orientation (e.g., Camenzind & Krockenberger 1992; Wagner & Witzel 1995; Bhatta et al. 2013; Marscher 2014, and the references therein). However, the exact details of the underlying processes are still under debate. In such context, the study of γ-ray variability of blazars provides us with an important tool to probe into jet dynamics and its associated particle acceleration and energy-dissipation mechanisms resulting in high-energy emission.

In blazars, the flux modulations due to disk processes could easily be swamped by the Doppler-boosted emission from jets. Nonetheless, the signatures of the disk modulations should, in principle, propagate along the jet through disk–jet coupling mechanisms such that the traces of characteristic timescales related to disk processes could be revealed through robust time-series analysis. Such timescales then can be linked to the various processes in the jet as well as the accretion disk such as dynamical, thermal, and viscous processes (Czerny 2006). For example, for blazars with typical masses between $\sim 10^8$ and $10^9\,M_\odot$, the dynamical, thermal, and viscous timescales are on the order of a few hours to a few years. Besides, several AGN models predict quasi-periodic oscillations (QPOs) in the flux with characteristic timescales ranging from a few hours to a few years. For instance, in the scenario of *magnetic flux paradigm* (see Sikora & Begelman 2013), the magnetic field at the accretion disk threads the black hole in launching the jets in the AGN, and consequently, it gives rise to various magnetohydrodynamical instabilities at the disk-magnetosphere interface. These instabilities in turn can produce QPOs, which subsequently could propagate along modulating the jet emission and could be observed in the multifrequency observations, including γ-ray light curves. In a similar context, the highly polarized optical flare discovered by Bhatta et al. (2015) might be a signature of the dominance of the magnetic field near blazar cores, the so-called magnetically arrested disk scenario (see Narayan et al. 2003). In observations, detection of QPOs in various kinds of AGNs (including both radio-loud and radio-quiet) on various timescales has been reported in several works (see Bhatta et al. 2016b; Bhatta 2017, 2018, 2019, and the reference therein). In addition, QPOs have been observed to naturally develop in numerical studies involving simulations of parsec-scale relativistic jets (e.g., McKinney et al. 2012).

State-of-the-art telescopes and detectors have enabled us to obtain a fair comprehension of these fascinating sources. In spite of the efforts to understand them, the details of the processes including the nature of accretion processes, the disk–jet connection, and the role of the magnetic field in launching the jets are still elusive. In this context, the primarily motivation of the current work is to characterize the statistical properties of γ-ray variability in blazars. The sources form a dominant group of sources that prominently shine in the γ-ray band: the recent fourth *Fermi* Large Area Telescope source catalog contains about 60% of the γ-detected sources as the blazar class (The Fermi-LAT collaboration 2019). Therefore, the study of γ-ray emission from blazars can compliment similar studies on the origin and propagation of high-energy emission in the universe (see Madejski & Sikora 2016; Rieger 2019).

In this work, we carry out a systematic in-depth analysis of 20 blazars utilizing decade-long *Fermi*/LAT observations. In

Section 2, the sample of blazars and its physical properties are listed in Table 1. In addition, a data processing method for *Fermi*/LAT instrument is outlined. In Section 3, several approaches to the analysis that adopting various methods including fractional variability, flux distribution, power spectral density (PSD), and QPO are introduced, and the results of the analyses on the γ-ray light curves are also presented. Then, a discussion of the results along with their possible implications for the nature of γ-ray emission from the sources are presented in Section 4. Finally, we summarize our conclusions in Section 5. Additionally, one table and several figures resulting from the analyses appear in Appendices A–E.

2. Sample Sources and *Fermi*/LAT Data Processing

Source Sample: we included most of the *Fermi*/Third Source Catalog (3FGL; Acero et al. 2015) sources for which there could be a weekly flux with a significant test statistic (TS) value. The sources included in the study are generally γ-ray bright (mostly TeV blazars) and consist of 12 BL Lacs and 8 FSRQs. The source names, their 3FGL catalog name, source classification, R.A., decl., and redshift are presented in columns 1, 2, 3, 4, 5, and 6, respectively, of Table 1. Of the 20 sources, the source with the highest redshift is PKS 1502+106 with $z = 1.84$, and the closest one ($z = 0.03$) is Mrk 421.

The Large Area Telescope (LAT) on board *Fermi* Gamma-ray Space Telescope (*Fermi*) is one of the most useful instruments in the study of the universe in high energy. It is equipped with a large effective area (>8000 cm^2), wide field of view (>2 sr), and high angular resolution (<3°.5 around 100 MeV and <0°.15 above 10 GeV). The instrument continuously scans the sky every 90 minutes across a wide spectral energy range that spans 20 MeV to TeV energies (Atwood et al. 2009). However, for most of the practical purposes, the data analysis is limited between the range 100 MeV–300 GeV. This is because a large point-spread function (PSF) below the range and low-event statistics above the range might render unreliable results. For this work, the *Fermi*/LAT observations from the period 2008 August 4–June 22 (~10 yr) and in the 100 MeV–300 GeV energy range were considered for the analysis. The *Fermi*/LAT observations of the sources were processed following the standard procedures of the unbinned likelihood analysis.[3] In particular, *Fermi* Science Tools were used that made use of the *Fermi*/LAT catalog, Galactic diffuse emission model, and isotropic model for point sources.[4] As a first step, selections of the events were made using the *Fermi* tool *gtselect*, which selected only the events in a circular region of interest (ROI) of a 10° radius centered around the source. To minimize the contamination of γ-rays from the Earth limb, the zenith angle was limited to <90°. Similarly, the *Fermi* tool *gtmktime* was used to select good time intervals to ensure that the satellite was operating in the standard science mode so that only high-quality observations enter the final analysis. After creating an exposure map using *gtexpmap* and *gtltcube*, a source-model file was created using the Python application make3FGLxml.py.[5] Subsequently, the diffuse source response was calculated using the Galactic and extra-Galactic models of the diffuse γ-ray emission, namely, *gll_ iem v06.fit* and *iso_P8R2 SOURCE V6 v06.txt*. To generate the light curves, the data were binned in weekly bins and the task *gtlike* was run to carry out a maximum-likelihood analysis (Mattox et al. 1996). As one of the input parameters to the likelihood analysis, the spectral index of the source model was frozen to the average index value from the 3FGL catalog. With the set of parameters given in the input source models, the task attempts to maximize the probability that the models represent the observations by fitting all of the sources within the ROI and, consequently, compute the significance of the γ-ray events from the source. The maximum-likelihood test statistic, measuring the significance of a detection, is given as $TS = 2 \times (\log L_1 - \log L_0)$, where L_1 and L_0 represent the likelihood of the data given the model with and without a point source at the position, respectively. Then, the significance of a source detection can be expressed by $\sim\sqrt{TS}\,\sigma$ (Abdo et al. 2010a). In the current work, to ensure a robust analysis, only the observations with TS value >10 (equivalently $\gtrsim 3\sigma$) were included (see also Bhatta 2017, 2019).

3. Analysis

In order to constrain the statistical variability properties of the blazars, the γ-ray light curves of the sample sources were intensively studied applying various analysis methods including fractional variability, flux distribution, rms–flux relation, and symmetry analysis. Moreover, time-series analysis in the form of power spectral density analysis, Lomb–Scargle periodogram, and weighted wavelet z-transform were carried out along with an extensive Monte Carlo (MC) simulations. The description of methods and the corresponding results of the analyses are presented below.

3.1. Fractional Variability

The decade-long light curves (e.g., see Figures 1, 5, and 9), distinctly revealing the variable nature of the sources, imply that the sources might have undergone dramatically violent episodes to result in the observed large flux variation over the period. The average variability during the entire period can be quantified by estimating their fractional variability (FV; a measure of normalized excess variance) given as

$$F_{\rm var} = \sqrt{\frac{S^2 - \langle\sigma_{\rm err}^2\rangle}{\langle F\rangle^2}}, \tag{1}$$

for which the uncertainty can be expressed as

$$\sigma_{F_{\rm var}} = \sqrt{F_{\rm var}^2 + \sqrt{\frac{2}{N}\frac{\langle\sigma_{\rm err}^2\rangle^2}{\langle F\rangle^4} + \frac{4}{N}\frac{\langle\sigma_{\rm err}^2\rangle}{\langle F\rangle^2}F_{\rm var}^2}} - F_{\rm var} \tag{2}$$

(Vaughan et al. 2003, see also Bhatta & Webb 2018). The resulting FVs for the sample sources are listed in the seventh column of Table 1. The analysis shows that the blazar light curves display remarkable variability in the γ-ray band with a mean (of the sources in the sample) FV of 73.37%—the mean FV of BL Lacs is 58.44% with a standard deviation of 24.83% and that of the FSRQs is 95.76% with a standard deviation of 16.03%. Of the sample sources, the most variable source is FSRQ CTA 102 ($z = 1.037$) with FV ~ 117%. Similarly, the next most variable sources are FSRQ 4C+21.35 and BL Lac TON 0599 with FV ~ 115% and ~111%, respectively. The least variable source turns out to be BL Lac W Comae with just

[3] https://fermi.gsfc.nasa.gov/ssc/data/analysis/scitools/likelihood_tutorial.html
[4] https://fermi.gsfc.nasa.gov/ssc/data/analysis/scitools/
[5] https://fermi.gsfc.nasa.gov/ssc/data/analysis/user/make3FGLxml.py

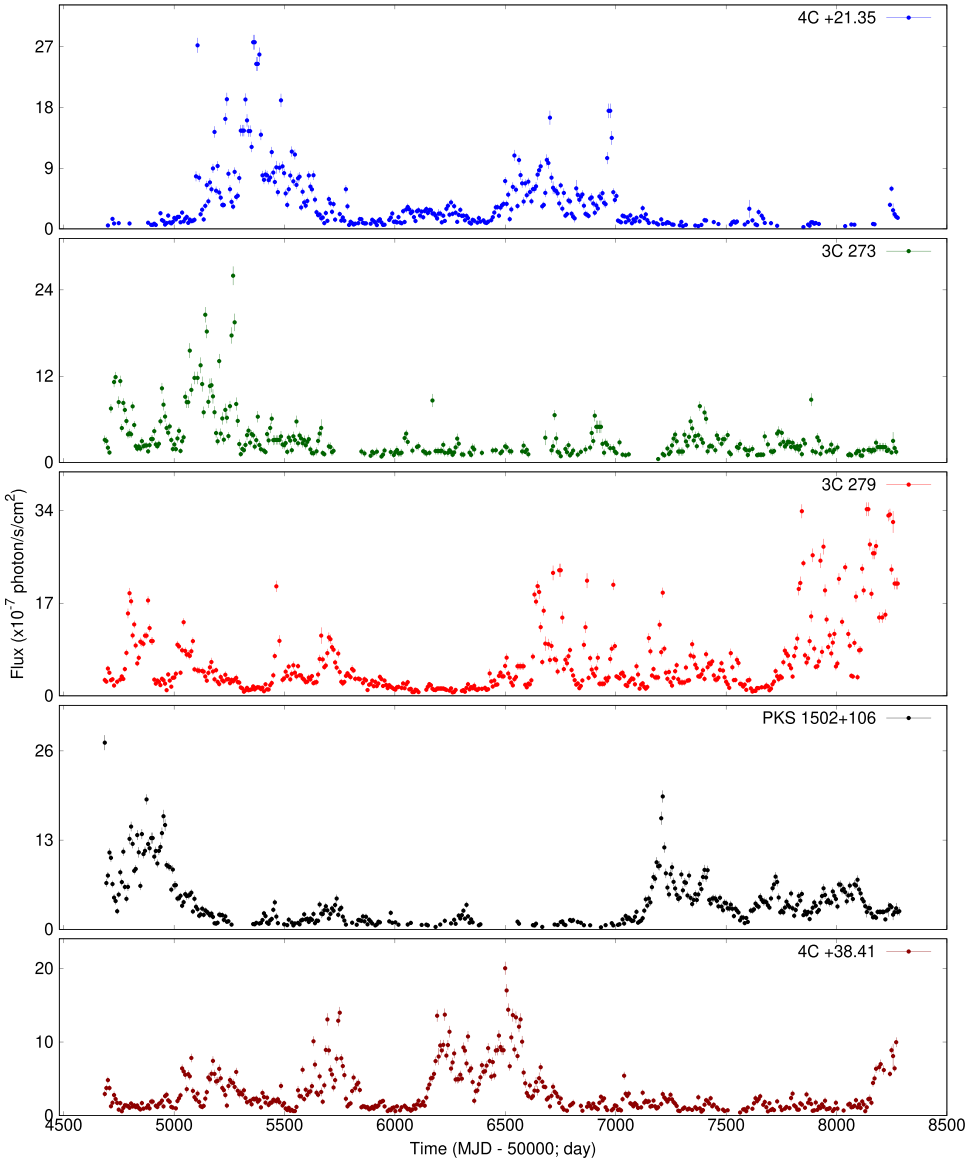

Figure 1. Weekly binned *Fermi*/LAT light curves of five well-studied blazars. The light curves for the remaining sources in the sample, as listed in Table 1, are presented in Appendix A.

FV $\sim$ 25%, followed by another BL Lac Mrk 501 with FV $\sim$ 33%. Although it appears that, in general, FSRQs sources are more variable than BL Lac sources in the sample, the analysis should be carried out on larger sample to obtain a more robust conclusion.

As an attempt to characterize the variability of the properties of the sources, we also studied the correlation between the FV and the spectral indexes of the sources taken from the 3FGL catalog. In particular, the Pearson linear correlation coefficient between the parameters turned out to be 0.61 with a p-value of 0.004. The plot between FV and the spectral index is shown in the left panel of Figure 2. In the figure, BL Lacs and FSRQs are shown in blue and red, respectively, and the best linear fit, with a coefficient of determination (R^2) = 0.3701 and p-value = 0.004, is represented by the black line. The fit results in a steep slope of $\sim$70, signifying high sensitivity of variability on the spectral index. Although the sample is small, it suggests a positive correlation between the quantities and encourages us to carry out similar future studies involving a larger number of sources. Among the sources, two outliers are easily distinguished visually: FSRQ 3C 454.3, with a flatter spectral index and high variability, and BL Lac W Comae, with a steeper index and the lowest FV.

3.2. Flux Distribution: Log-normality and Rms–Flux Relation

A study of the long-term flux distribution of blazars can hold some of the important clues to the origin and nature of their variability. In particular, a statistical probe of probability density function (PDF) of gamma-ray flux can provide important insights on the nature of high-energy emission processes, and thereby help constrain the underlying processes that drive observed variability in blazars. With such a goal, we studied the γ-ray flux distribution of the blazar samples by constructing histograms to ascertain PDFs of the distribution, which can be approximated by the model fit to the distribution of the fluxes from the long-term light curves. We mainly attempted to fit normal and log-normal PDFs.

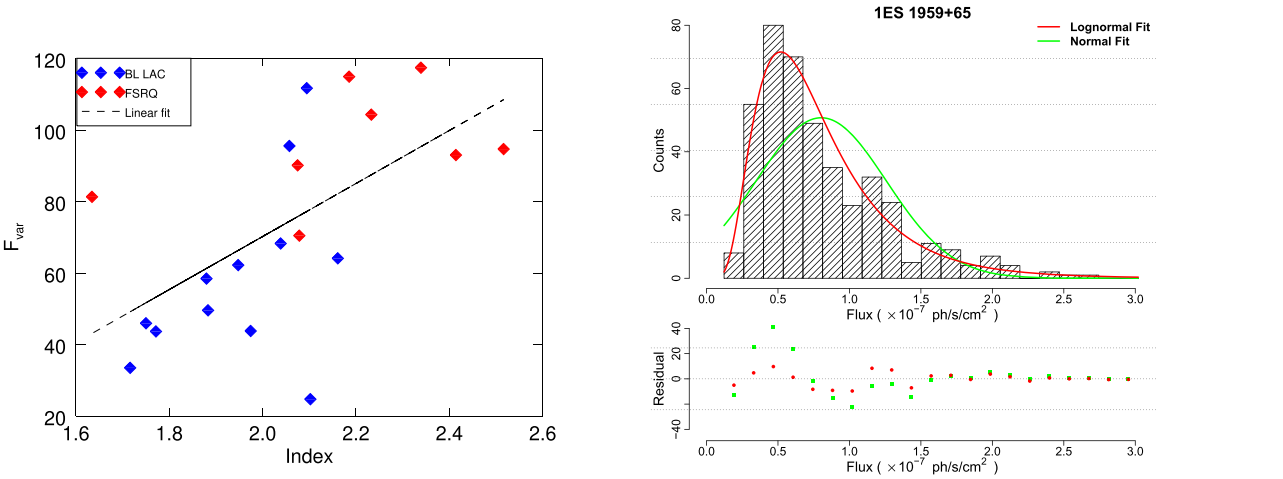

Figure 2. Left panel: fractional variability plotted against corresponding *Fermi*/LAT band spectral indexes of the sources. BL Lacs and FSRQs are shown by the blue and red symbols, respectively, and the black line shows the best linear fit to the data. Right panel: γ-ray flux distribution (hatched black), and normal (green) and log-normal (red) PDF fitting to the histogram of the source 1ES 1959+65. Similar plots for other sources are presented in Appendix C.

A normal distribution is defined by

$$f_{\rm normal}(x) = \exp\left(-\frac{(x-\mu)^2}{2\sigma^2}\right), \quad (3)$$

where μ and σ are the mean and the standard deviation of the normal distribution, respectively, expressed in units of flux, i.e., counts s^{-1} cm^{-2}. Similarly, a log-normal distribution is defined by

$$f_{\rm lognormal}(x) = \frac{1}{xs\sqrt{2\pi}}\exp\left(-\frac{(\ln x - m)^2}{2s^2}\right), \quad (4)$$

where m and s are the mean location and the scale parameters of the distribution, respectively, and m is expressed in units of the natural log of flux.

First, we performed curve fitting to the flux histograms of the sample sources using the above two PDFs by employing the weighted least-square (WLS) method on the binned data, and the resulting fit statistics for both log-normal and normal PDFs are listed in Appendix B. The mean of the flux, scale, and reduced χ^2 for the log-normal fitting are listed in columns 2, 3, and 4, respectively. Similarly, the mean, standard deviation, and reduced χ^2 for the normal fitting are presented in columns 5, 6, and 7, respectively. Based on the reduced χ^2, i.e., χ^2/dof, we find that, for most of the sources, the log-normal PDF fits better than the normal PDF. However, in sources AO 0235 +164, ON+325, BL Lac, and 3C 454.3, the reduced χ^2 values for both of the PDFs are comparable, and the normal distribution fits provide a slightly better representation. We also studied the flux distribution using a more robust maximum-likelihood estimation (MLE) method, and implemented the PDF fitting using the software package *fitdistrplus*[6] (Delignette-Muller & Dutang 2015) available in the MASS library of the public domain R statistical software system. The package attempts to fit PDFs to the unbinned flux distribution using MLE method, as opposed to the PDF fitting on the binned histogram in WLS method. The resulting fit statistics along with the log-likelihood (LL), Bayesian information criterion (BIC), and Akaike information criterion (AIC) quantities for the sample sources are presented in Table 2. The smaller AIC and BIC values for the log-normal PDF suggest that, compared to the normal PDF, it is a more preferable representation of the blazar flux distribution. Histogram fits to the source 1ES 1959+65 using normal and log-normal distributions and the corresponding residuals are shown in the right panel of Figure 2, and similar plots for the remaining sources in the sample are presented in Appendix C. From the figures, it is evident that the observed flux distribution is asymmetric with a heavy tail.

We further tried to characterize the flux distribution and variability properties by investigating the correlation between the flux states and source activity as represented by the root mean square (rms), commonly known as *rms–flux relation*. For this purpose, the light curves were divided into N segments of equal lengths such that each segment contains at least 20 observations. This is to ensure that we can conduct a meaningful statistical analysis. For each segment of the light curve, the Poisson noise-corrected excess variance is given as $\sigma_{XS}^2 = S^2 - \bar{\sigma}_{\rm err}^2$, where S^2 represents the sample variance and $\bar{\sigma}_{\rm err}^2$ is the mean square of the measurement error given by $\bar{\sigma}_{\rm err}^2 = 1/n\sum_i^n \sigma_{{\rm err},i}^2$. From the light curve of the source 3C 279, the rms values for each segment are plotted against the corresponding mean flux values in left panel Figure 3. The magenta line in the figure represents the linear fit to the observations and also serves as a visual guide to the trend that appears on the rms–flux plane. Similar figures for rest of the sample sources are presented in Appendix C. We see that a linear trend distinctly appears in most of the sources. The slope parameters from the linear fit are listed in the second column of Table 3. The mean slope of the sources is 0.47; BL Lac ON +325 has the flattest slope of 0.03, whereas another BL Lac TON 0599 shows the steepest slope 0.82. It can be seen that, in general, BL Lacs shows a flatter average slope 0.43 in comparison to the steeper average slope of 0.56 for FSRQs. To further quantify the correlation between the rms and flux in the sources, Spearman rank correlation coefficients are estimated along with the corresponding p-values that represent the two-sided significance of its deviation from zero, which are presented in the third and fourth columns of the table, respectively. As the p-values indicate, the linear correlation between the flux and rms seems to be a dominant trend in most of the sample sources. It is important to note that, except for the

[6] https://cran.r-project.org/web/packages/fitdistrplus/index.html

Table 2
Log-normal and Normal Distribution Fit Statistics for the γ-Ray Flux Distribution of the *Fermi*/LAT Sources Using the Maximum-likelihood Estimation Method

	Log-normal Fit					Normal Fit				
Source Name (1)	m (2)	s (3)	LL (4)	AIC (5)	BIC (6)	μ (7)	σ (8)	LL (9)	AIC (10)	BIC (11)
3C 66A	-0.03 ± 0.02	0.52 ± 0.02	-369	743	751	1.12 ± 0.03	0.70 ± 0.02	-526	1057	1065
AO 0235+164	0.43 ± 0.05	0.78 ± 0.03	-439	882	889	2.16 ± 0.13	2.09 ± 0.09	-588	1181	1188
PKS 0454−234	0.72 ± 0.03	0.71 ± 0.02	-848	1700	1708	2.61 ± 0.08	1.82 ± 0.06	-952	1909	1917
S5 0716+714	0.60 ± 0.03	0.68 ± 0.02	-799	1602	1610	2.25 ± 0.06	1.43 ± 0.05	-870	1745	1753
Mrk 421	0.65 ± 0.02	0.41 ± 0.01	-603	1210	1218	2.09 ± 0.04	0.96 ± 0.03	-699	1403	1411
TON 0599	0.35 ± 0.04	0.77 ± 0.03	-536	1077	1084	2.02 ± 0.12	2.28 ± 0.09	-796	1597	1605
ON +325	-0.32 ± 0.03	0.64 ± 0.02	-289	581	590	0.86 ± 0.02	0.51 ± 0.02	-331	666	674
W Comae	-0.49 ± 0.03	0.40 ± 0.02	-3	11	18	0.66 ± 0.02	0.29 ± 0.01	-35	74	80
4C +21.35	0.91 ± 0.05	0.97 ± 0.04	-854	1712	1720	4.02 ± 0.24	4.63 ± 0.17	-1101	2206	2214
3C 273	0.96 ± 0.04	0.69 ± 0.03	-727	1459	1466	3.45 ± 0.17	3.31 ± 0.12	-950	1904	1911
3C 279	1.39 ± 0.04	0.87 ± 0.03	-1342	2688	2696	6.02 ± 0.28	6.30 ± 0.20	-1637	3277	3286
PKS 1424−418	1.52 ± 0.03	0.68 ± 0.02	-1203	2410	2418	5.69 ± 0.19	4.04 ± 0.13	-1332	2667	2676
PKS 1502+106	1.01 ± 0.04	0.87 ± 0.03	-878	1760	1768	3.93 ± 0.18	3.57 ± 0.13	-1033	2071	2078
4C +38.41	0.81 ± 0.04	0.81 ± 0.03	-937	1877	1886	3.20 ± 0.14	3.01 ± 0.10	-1164	2332	2340
Mrk 501	-0.63 ± 0.02	0.45 ± 0.01	7	-10	-1	0.59 ± 0.01	0.25 ± 0.01	-20	44	52
1ES 1959+65	-0.37 ± 0.03	0.54 ± 0.02	-182	369	377	0.80 ± 0.02	0.46 ± 0.02	-266	536	544
PKS 2155−304	0.08 ± 0.02	0.47 ± 0.01	-383	769	778	1.21 ± 0.03	0.61 ± 0.02	-467	939	947
BL Lac	1.08 ± 0.03	0.66 ± 0.02	-991	1987	1995	3.63 ± 0.11	2.38 ± 0.08	-1085	2175	2183
CTA 102	1.58 ± 0.05	1.08 ± 0.04	-1309	2623	2631	8.66 ± 0.49	10.18 ± 0.35	-1589	3182	3190
3C 454.3	2.25 ± 0.05	1.00 ± 0.03	-1694	3392	3401	14.11 ± 0.53	11.49 ± 0.38	-1784	3571	3580

Note. Similar table using the weighted least-squares method is presented in Appendix B. For the normal fit, μ and σ are presented in units of flux in $10^{-7} \times$ counts s^{-1} cm^{-2}, whereas for the log-normal fit m is in units of natural log of flux.

source ON +325, all of the sources in the sample display a strong linear rms–flux relation. Similar results were reported in the work of Kushwaha et al. (2017), who studied the *Fermi*/LAT observations of four AGNs.

3.3. Symmetry Analysis: Flux Rise and Decay Profiles

To investigate the nature of the particle acceleration that results in the flux rise and energy-dissipation mechanism causing flux decay in a source light curve, the distribution of positive and negative flux rates is studied by considering two consecutive fluxes in the light curve. Such a statistical analysis, in principle, should reveal the inherent difference between the nature of acceleration and cooling mechanisms. To carry out the analysis, flux rates between two fluxes consecutive in time were estimated at rate $= \Delta F/\Delta t$. This provides a simple measure of how swiftly the fluxes rise or decay in the weekly time bin. A comparison between the rise and decay rates (positive and negative rates, respectively) in all of the sources in the sample is presented in Table 4. Here, for each of the sources, the ΔFs are normalized by the mean flux of the entire light curve so that the flux change rates can be expressed in percent per day and thereby be conveniently compared with the values for the other sources in the sample. We find that the positive and negative flux change rates for each of the sources in the sample, as listed in the second and third columns of the table, are very similar. As an illustration, the flux rise and decay rates against the mean flux for the source S5 0716+714 are plotted in the right panel of Figure 3. It is interesting to note that a similar conclusion was inferred in Abdo et al. (2010a), who studied a similar large number of sources in the *Fermi*/LAT observations. Furthermore, in order to see how similar/dissimilar the distribution of decay rates from the rise rates is, a Kolmogorov–Smirnov (K-S) test was performed. The K-S statistic (D), listed in the fourth column of Table 4, specifies the maximum deviation between the cumulative distributions of the two samples. The p-value corresponding to the K-S statistic can be used to infer whether both samples can be considered as drawn from the same parent population. As indicated by the p-values in the fifth column of Table 4, none of the sources have flux rise and decay rates that are significantly different from each other.

Moreover, any two consecutive fluxes and their mean can be used to compute rise/decay timescales as given by

$$\frac{1}{\tau_{\pm}} = \pm \frac{\Delta F}{\Delta t} \frac{1}{\langle F \rangle}, \tag{5}$$

where $\Delta t = t_i - t_{i+1}$, $\Delta F = F_i - F_{i+1}$, and $\langle F \rangle = (F_i + F_{i+1})/2$. Note that this timescale can be taken as a measure for the flux-doubling timescale. The average of such timescales along with the corresponding 1σ are listed in the sixth column of Table 4. We find that in almost all sources, the flux rise and decay timescales are very similar, which are on the order of a few weeks.

3.3.1. Time-series Analysis

Power spectral density. The discrete Fourier periodogram (DFP) of a light curve of a variable source provides a measure for the variability power at a given temporal frequency (or, equivalently, timescale). Mathematically, it can be given by the square of the absolute value of discrete Fourier transform. For a time series $x(t_j)$ sampled at times t_j with $j = 1, 2, .., n$ and spanning a total duration of observations, T, the DFP at a

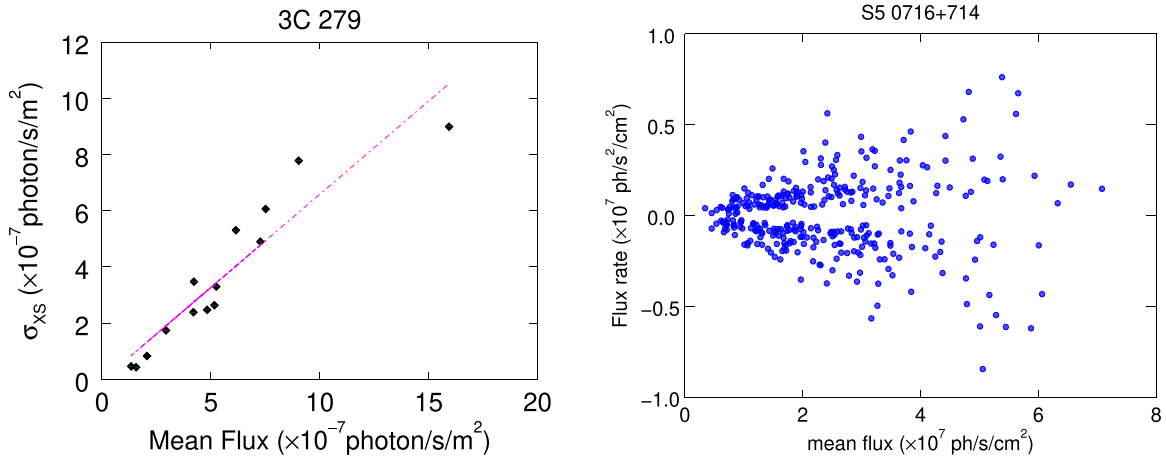

Figure 3. Left panel: rms–flux relation in the FSRQ 3C 279. The magenta line represents the linear fit to the observations. Similar figures for other sources are presented in Appendix D. Right panel: distribution of rates of flux changes over the mean of the consecutive fluxes of the BL Lac S5 0716+714.

Table 3
Relation between Rms and the Mean Flux of γ-Ray Light Curves of the *Fermi*/LAT Blazars

Source (1)	Slope (2)	Spearman's r. c. (ρ) (3)	p-value (4)
3C 66A	0.70	0.73	0.006
AO 0235+164	0.59	0.94	<0.001
PKS 0454−234	0.47	0.73	0.007
S5 0716+714	0.39	0.93	0.006
Mrk 421	0.65	0.78	0.001
TON 0599	0.82	0.94	<0.001
ON +325	0.03	0.04	0.09
W Comae	0.22	0.80	0.02
4C +21.35	0.61	0.86	<0.001
3C 273	0.77	0.90	<0.001
3C 279	0.66	0.96	<0.001
PKS 1424−418	0.25	0.71	0.004
PKS 1502+106	0.46	0.96	<0.001
4C+38.41	0.48	0.96	<0.001
Mrk 501	0.39	0.68	0.007
1ES 1959+65	0.32	0.85	0.002
PKS 2155−304	0.39	0.68	0.007
BL Lac	0.35	0.78	<0.001
CTA 102	0.52	0.95	<0.001
3C 454.3	0.42	0.90	<0.001

temporal frequency ν is expressed as

$$P(\nu) = \frac{1}{n}\left|\sum_{j=1}^{n} x(t_j)\, e^{-i2\pi\nu t_j}\right|^2 . \quad (6)$$

The periodograms are computed for $n/2$ frequencies that are evenly sampled in log-space between the minimum $\nu_{\rm min} = 1/T$ and $\nu_{\rm max} = 1/2\Delta t$, where Δt is the mean sampling step in the light curve. Moreover, the periodogram can be normalized to express it in convenient units. In particular, if we normalize it with a factor $2T/(n\bar{x})^2$, the unit becomes $(\mathrm{rms/mean})^2/\mathrm{day}$. The main advantage of this normalization is that the total integrated power of the periodogram is nearly equal to the variance of the light curve—a result following from Parseval's theorem. The distribution of the DFP over the temporal frequencies reveals variability power at corresponding timescales and thereby provides information about the underlying variability structures and dominant timescales. A PSD is a mathematical function that best approximates the shape of a source periodogram. In general, blazar periodograms have been found to be best approximated by power-law functions of the form $P(\nu) \propto \nu^{-\beta}$ with a spectral power index β. However, in reality, a true underlying PSD of a source light curve sampled at discrete times for a finite duration often gets distorted by the effects of the sampling pattern as represented by the window function. Therefore, it is important that any robust evaluation of the PSD of real astronomical observations should be able to carefully untangle the effects of the window function on the observed PSD.

The Power Spectrum Response method (PSRESP; Uttley et al. 2002) is one such method that is frequently applied in the characterization of a PSD of AGN periodogram (see Bhatta et al. 2016b, 2018; Bhatta 2019, and the references therein). The main merits of the method are that it properly accounts for a number of important issues relating to the blazar light curves, such as dominant red noise, discrete sampling, finite observation length, and uneven sampling of the light curve. Moreover, since the nature of the distribution of periodograms of unevenly spaced light curves of power-law-type PSDs is not well understood, the distribution of a large number of simulated light curves (that posses similar statistical properties such as mean, standard deviation, sampling pattern, and observation duration) is utilized to compute a measure for the goodness of fit of a model PSD.

As mentioned earlier, the sampling properties of the observed light curve can impose distorting effects on the true underlying PSD in many ways. In particular, variability power leakage from lower to higher frequencies owing to the limited observation period (commonly known as red noise leakage) can alter the true PSD shape by flattening the high-frequency tail of the power-law function (Papadakis & Lawrence 1993). During the spectral analysis of the blazar PSD, the effects of the red noise leak were corrected through extensive MC simulations. Particularly, to address this issue within the scheme of the PSRESP, light curves were first simulated 10 times longer than the total source observation duration and then divided into segments of 10 data sets (Isobe et al. 2015). Similarly, in the case of the light curve with the finite time resolution (or inadequate sampling rate), *aliasing* can alter the shape of the PSD and also lead to the flattening of the

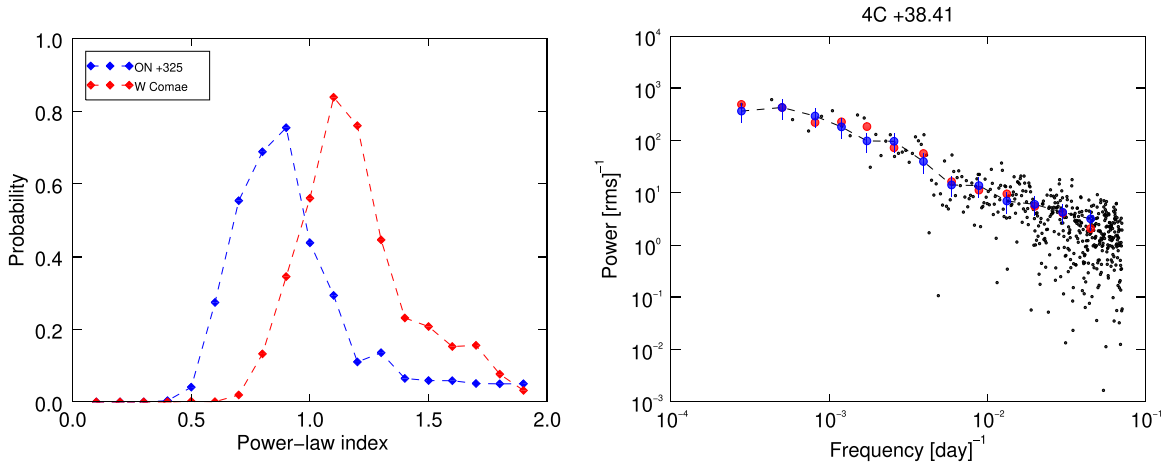

Figure 4. Left panel: following PSRESP, the distribution of the probability that the given power-law PSD model best represents the source periodograms is plotted over spectral indexes ranging from 0 to 2 for W Comae (red) and ON +325 (blue). Right panel: discrete Fourier periodogram of the source 4C +38.41 (black), binned periodogram (red), and best-fit PSD (blue). Similar plots for the other sources are presented in Appendix E.

Table 4
Symmetry Analysis of γ-Ray Fluxes of the Source Light Curves

Source (1)	Rise Rate (% day^{-1}) (2)	Decay Rate (% day^{-1}) (3)	D (4)	p-value (5)	Ave. Timescale (days) (6)
3C 66A	7.28 ± 6.36	7.50 ± 7.23	0.12	0.33	17.51 ± 7.72
AO 0235+164	8.36 ± 6.51	7.85 ± 6.64	0.11	0.70	21.98 ± 21.67
PKS 0454−234	6.04 ± 5.61	5.76 ± 4.55	0.08	0.63	22.19 ± 11.90
S5 716+714	7.06 ± 5.92	7.11 ± 5.96	0.06	0.93	20.10 ± 13.02
Mrk 421	5.00 ± 3.16	5.00 ± 3.01	0.10	0.51	24.94 ± 12.22
TON 0599	7.39 ± 7.31	7.04 ± 7.15	0.10	0.55	20.61 ± 20.27
ON +325	10.62 ± 6.71	11.27 ± 7.78	0.09	0.71	11.84 ± 5.93
W Comae	5.82 ± 3.78	6.29 ± 5.05	0.12	0.92	31.72 ± 29.80
4C +21.35	8.45 ± 6.48	7.49 ± 6.50	0.15	0.13	21.74 ± 21.52
3C 273	8.82 ± 9.67	7.52 ± 6.21	0.11	0.52	21.98 ± 17.22
3C 279	7.77 ± 6.77	7.34 ± 8.83	0.09	0.51	21.55 ± 14.92
PKS 1424−418	3.77 ± 2.88	4.07 ± 3.25	0.11	0.25	32.22 ± 19.14
PKS 1502+106	4.98 ± 4.05	5.66 ± 5.82	0.08	0.84	28.14 ± 27.89
4C +38.41	6.52 ± 6.49	6.44 ± 6.17	0.06	0.93	22.34 ± 15.19
Mrk 501	7.52 ± 3.65	7.48 ± 3.77	0.06	0.97	16.21 ± 7.78
1ES 1959+65	7.23 ± 4.26	7.73 ± 4.74	0.11	0.70	17.29 ± 9.74
PKS 2155−304	6.13 ± 3.96	6.77 ± 4.11	0.11	0.28	19.18 ± 9.02
BL Lac	6.40 ± 4.96	6.28 ± 5.01	0.08	0.69	20.44 ± 11.96
CTA 102	6.30 ± 6.19	6.55 ± 6.13	0.10	0.42	23.59 ± 20.87
3C 454.3	4.99 ± 4.63	4.87 ± 4.97	0.08	0.60	30.86 ± 22.03

high-frequency tail of the true PSD. The effect, in general, can be avoided by sampling the periodogram up to the Nyquist frequency (see Uttley et al. 2002).

To implement PSRESP,[7] 10,000 light curves with a 7 day bin were simulated using single power-law PSD model with a spectral power index β as given by $P(\nu) = \nu^{-\beta} + C$ (see Timmer & Koenig 1995). The simulated light curves were assigned the same observational properties, e.g., mean, standard deviation, observational length, and uneven sampling, and consequently, periodograms for each simulated light curve were computed. The distribution of simulated periodograms in turn was then utilized to estimate the best-fit PSDs for the source γ-ray light curves. In the left panel of Figure 4, the probability distribution over the spectral index is presented for the sources W Comae (red) and ON +325 (blue). The figure shows that the spectral indexes corresponding to the best-fit PSD are 1.10 ± 0.09 (W Comae) and 0.84 ± 0.14 (ON +325), where the half width at half maximum from the Gaussian fit to the observations is used to represent the uncertainties in the indexes. Following a similar procedure, spectral indexes corresponding to the best-fit PSD model for the sample sources are listed in the eighth column of Table 1. In addition, figures showing the DFP (black), binned periodogram (red), and the best-fit PSD model (blue) for the sample sources are presented in Appendix E, whereas the plot showing the best-fit PSD for the source 4C+38.41 is presented in the right panel of Figure 4.

It is found that the periodograms of γ-ray light curves of the 20 sources are consistent with a single power law of the form $P(\nu) \propto \nu^{-\beta}$ where the slope index ranges between 0.8 and 1.5. The mean PSD index of all of the sources in the sample turns out to be 1.13 with a standard deviation of 0.18. To compare between FSRQs and BL Lacs, the mean index for BL Lacs is

[7] We have described the PSRESP method and its implementation in detail in several of our previous works, Bhatta et al. (2016a, 2016b) and Bhatta (2017, 2019).

Table 5
List of the Blazars in the Sample That Show Significant QPO in the γ-Ray Light Curves

	LSP		WWZ			
Source (1)	Period (days) (2)	Local Sig. (%) (3)	Global Sig. (%) (4)	Period (days) (5)	Local Sig. (%) (6)	Global Sig. (%) (7)
S5 716+714	346 ± 23	99.97	99.96	349 ± 27	99.982	99.980
Mrk 421	285 ± 27	99.99	99.97	287 ± 32	99.997	99.993
PKS 2155−304	610 ± 51	99.9994	99.99841	617 ± 53	99.995	99.9981
PKS 1424−418	353 ± 21	99.98	99.95	349 ± 24	99.985	99.981
ON +325	1086 ± 63	99.9986	99.9968	1081 ± 67	99.987	99.983

1.05 with a standard deviation 0.17, whereas the mean of FSRQs is 1.24 with a lesser spread in standard deviation of 0.13. The results also show that the source with the steepest index, 1.5, is PKS 1424−418, whereas the source with the flattest index turns out to be ON +325. Our results are in close agreement with the recent results of 1.15 ± 0.10 obtained by Meyer et al. (2019) and are also largely in agreement with the work of Nakagawa & Mori (2013) using 4 yr long *Fermi*/LAT observations of 15 sources. However, in a study of the first 11 months of the *Fermi* survey involving several blazars, Abdo et al. (2010a) reported steeper average slope indexes of 1.5 for FSRQs and 1.7 for BL Lacs. These discrepancies can be ascribed to the differences in methods, sampling intervals, and total observation durations between the two works.

Quasi-periodic oscillations. As we saw above, the periodograms of source light curves can be largely characterized by a single power-law PSD. But if we closely look at the periodogram structures, occasionally we find peaks at some frequencies suggesting the possible presence of (quasi-) periodic signals in the observations. In fact, several sources are known to show QPOs in their light curves in different energy bands (see Bhatta et al. 2016b; Gupta 2018, and the references therein). To cite a few cases, blazar OJ 287 is famous for showing characteristic double-peaks in its optical light curve that reoccur after every ∼12 yr (e.g., Sillanpää et al. 1988). In the γ-ray energy band, the first case of year-scale QPO was observed in blazar PG 1153+113, which seemed to display a ∼2 yr periodic modulation in the *Fermi*/LAT observations (see Ackermann et al. 2015). Subsequently, a number of works have reported QPOs in the γ-ray light curves of several blazars, e.g., ∼230 days QPO in Mrk 501 (Bhatta 2019), 34.5 days in PKS 2247−131 (Zhou et al. 2018), ∼2 yr in PKS 0301−243 (Zhang et al. 2017c), and 3.35 yr in PKS 0426−380 in Zhang et al. (2017b). In addition to these QPO studies focused on individual sources, the search for QPOs in γ-ray light curves in a sample of γ-ray bright sources has also been carried out in several works (e.g., see Sandrinelli et al. 2014, 2016a, 2017; Ait Benkhali et al. 2020).

The periodic γ-ray flux modulations most likely originating in the blazar jets can, through long-memory processes, carry information about the violent processes occurring at the innermost regions of AGNs. At a time when the central engines of AGNs still cannot be resolved by most of our current instruments, time-series analyses carrying out studies of QPOs can serve as probes into the nature of the disk–jet connection and jet ejection. With such a motivation, we analyzed the decade-long γ-ray observations of the sample source applying the Lomb–Scargle periodogram (LSP; Lomb 1976; Scargle 1982), one of the most efficient methods of finding QPO signals in the data with irregularities and gaps. The method basically tries to obtain a least-squares fit for sine waves of the form $X_f(t) = A\cos\omega t + B\sin\omega t$ to the observations such that the periodogram is given according to

$$P = \frac{1}{2}\left\{\frac{\left[\sum_i x_i \cos\omega(t_i-\tau)\right]^2}{\sum_i \cos^2\omega(t_i-\tau)} + \frac{\left[\sum_i x_i \sin\omega(t_i-\tau)\right]^2}{\sum_i \sin^2\omega(t_i-\tau)}\right\}, \quad (7)$$

where τ is given by $\tan(2\omega\tau) = \sum_i \sin\omega t_i / \sum_i \cos\omega t_i$. The periodogram is evaluated for N_ν number of frequencies between the minimum, $\nu_{\min} = 1/T$, and the maximum frequencies, $\nu_{\max} = 1/(2\Delta t)$. The total number of frequencies can be empirically given as $N_\nu = n_0 T \nu_{\max}$, where n_0 can be chosen in the range of 5–10 (see VanderPlas 2018). A peak centered at a temporal frequency may potentially suggest the presence of a periodic signal characteristic to the corresponding timescale. Unlike strictly periodic signals, which appear as sharp peaks in the periodogram, QPO signals give rise to periodogram structures that are extended over the frequencies nearby a central characteristic frequency. In the case of the real astronomical observations that often show irregular sampling and gaps in the data, spurious peaks can arise due to a number of factors that are discussed in this Section. More importantly, in blazar light curves, which are dominated by variability due to red-noise processes, high-amplitude QPO features can arise especially in the lower-frequency region of the periodograms. Therefore, any significance-estimation method should take into account this behavior along with the other artifacts that are prevalent in finite-duration time series sampled at discrete and irregular time steps—in other words, artifacts introduced by a window function.

To further explore the transient (in frequency and amplitude) nature of the possible QPOs, we also performed weighted wavelet z-transform (WWZ), one of the robust wavelet methods (see Foster 1996, for details).[8] The decade-long γ-ray observations of the blazars were analyzed to search for possible periodic flux modulations using both the LSP and WWZ methods. The analyses suggested the presence of year-scale QPOs in some of the objects in the source sample, as listed in Table 5. The LSP diagram for these sources is presented in the left column panels of Figures 6 and 7. The corresponding WWZ diagrams are placed on the right column panels of those figures. Moreover, the significant periods that

[8] We are skipping some of the details here including the implementation of the method and the significance estimation, as we have extensively covered these topics in our multiple previous works (see Bhatta et al. 2016b; Bhatta 2017, 2019).

resulted from the LSP and WWZ methods are listed in the second and fifth columns of Table 5, respectively.

The significance of the detected periodogram features were computed by employing the PSRESP method during which extensive MC simulations were performed. In particular, the spectral distribution of 10,000 simulated light curves (simulated using their corresponding best-fit PSD models) were employed to evaluate the local 90% and 99% significance contours (see also Bhatta et al. 2016b, 2018; Bhatta 2017, 2019). The estimation of the local significance only makes the use of the simulated LSP distribution at the period of the detected QPO, whereas global significance, given that we do not have a priori knowledge of the period of the detection, considers the simulated spectral distribution at all of the temporal frequencies considered (see Bell et al. 2011; Bhatta 2017, for details). The resulting 90% (magenta) and 99% (red) significance contours in the LSP diagram are presented in the left column panels of Figures 6 and 7, and the local and global significances of dominant periods are listed in the third and fourth columns, respectively, of Table 5. Similarly, the 99% significance contours are shown in the WWZ plots as red curves, and the local and global significances of dominant periods are listed in the sixth and seventh columns, respectively, of the table. Moreover, a brief description of each of the sources showing possible QPO features is presented below.

1. S5 0716+714: We detected highly significant QPOs at the period centered around 340 days. The tentative peaks of the periodic oscillation are marked in the source light curve with vertical lines at a separation of ∼340 days as shown in panel (a) of Figure 5. The LSP (left panel) and WWZ (right panel) diagrams along with the corresponding significance contours are presented in panel (a) of Figure 6. It is interesting to note that Prokhorov & Moraghan (2017) in their analysis including the *Fermi*/LAT observations from 2008 to 2016 also detected exactly the same periodicity with a high significance (99%) over the power law. However, in their work, Sandrinelli et al. (2017) did not detect the QPO. It should be pointed out that, in addition to 346 day QPO, the 1002 day QPO—possibly the third harmonic—also appears to be significant (>99%) in both of the analyses. But in such case, the light curve would contain only three cycles, which would leave one uncertain as to the realness of the signal. Interestingly, this period is close to that of the optical QPO detected by Raiteri et al. (2003), with the possible interpretation that the γ-ray QPO could be the counterpart of the optical one.
2. Mrk 421: With a significance greater than 99%, we detected ∼280 days periodic flux modulations in the famous blazar Mrk 421. Both the LSP and WWZ diagrams of the source are presented in panel (b) of Figure 6, and additionally, the tentative peaks of the oscillations are marked with the vertical lines drawn at intervals nearly equal to the period as shown in panel (b) of Figure 5. The detection supports the previous claim by Li et al. (2016), who reported the exact same period in the γ-ray band along with the similar one in 15 GHz radio observations. Similarly, Benitez et al. (2015) reported a similar period of 310 days in the multifrequency (optical, hard X-ray, and γ-ray) light curves of the source. However, in the analysis presented by Sandrinelli et al. (2017), it was not found to be significant enough.
3. PKS 2155−304: We detected ∼610 day periodic flux oscillations in the blazar PKS 2155−304. The WWZ analysis reveals that over the year, the period is gradually shifting toward a slightly higher frequency. We show the tentative peaks of the oscillation of the period, which are marked with vertical lines in panel (d) of Figure 5. The source LSP and WWZ spectral powers along with the significance contours are shown in panel (c) of Figure 6. A number of previous works have also reported similar periods, e.g., 700 days in the optical and γ-ray (Chevalier et al. 2019), 620 days in the γ-ray (Ait Benkhali et al. 2020), 635 days in the γ-ray (Zhang et al. 2017a), 640 days in the γ-ray (Sandrinelli et al. 2016), and 625 days in the lower energy band (300 MeV–1 GeV) of the *Fermi*/LAT light curve (Sandrinelli et al. 2014). Also, it is intriguing to note that this timescale is nearly double the 317 day timescale reported by Zhang et al. (2014) for the light curves spanning 35 yr using multiple methods such as epoch folding, the Jurkevich periodogram, and a discrete correlation function. The optical QPO was also reported in Sandrinelli et al. (2014). In addition, we also detected an ∼260 day QPO with a high significance (>99.99% using both the methods); although, the flux oscillations of the period are not visually clear in the light-curve plot.
4. PKS 1424−418: We found 353 days periodic flux oscillations in the γ-ray flux of the source blazar PKS 1424−418 significant above 99% over the power-law noise. The possible QPO appearing in several cycles in the data is reported here for the first time. The LSP and the WWZ diagrams along with the respective significance contours are shown in panel (e) of Figure 7; also, the tentative peaks of the periodic oscillations are shown with vertical lines in panel (d) of Figure 5.
5. ON +325: Both the LSP and WWZ analyses of the ON +325 light curve resulted in the detection of a significant periodic oscillation with characteristic timescales of ∼1070 days. However, since only three cycles can be seen in the entire light curve, it is not clear if it is truly a segment of QPO oscillations. We drew the tentative peaks of the oscillations of the period, which are marked with vertical lines in panel (c) of Figure 5, and the distributions of LSP and WWZ powers of the source are shown in panel (e) of Figure 7. It is noted that a ∼4.5 yr optical QPO was claimed in the source previously (Fan et al. 2002).
6. BL Lac: As shown in panel (f) of Figure 7, the structure of the LSP and WWZ power distributions of the source appears to be rather complex. There does not seem to be one dominant sinusoidal component, but there are a number of possible timescales, in particular ∼270, 520, and 750 days. Note that the first two periods are close to the harmonic range. However, these peaks are well below the 99% contour and, therefore, cannot be considered significant. We note that the 680 day γ-ray QPO claimed in the work of Sandrinelli et al. (2017) is not visible in the analysis.
7. In addition, a ∼330 day period QPO in the TeV blazar Mrk 501 has been reported in Bhatta (2019).

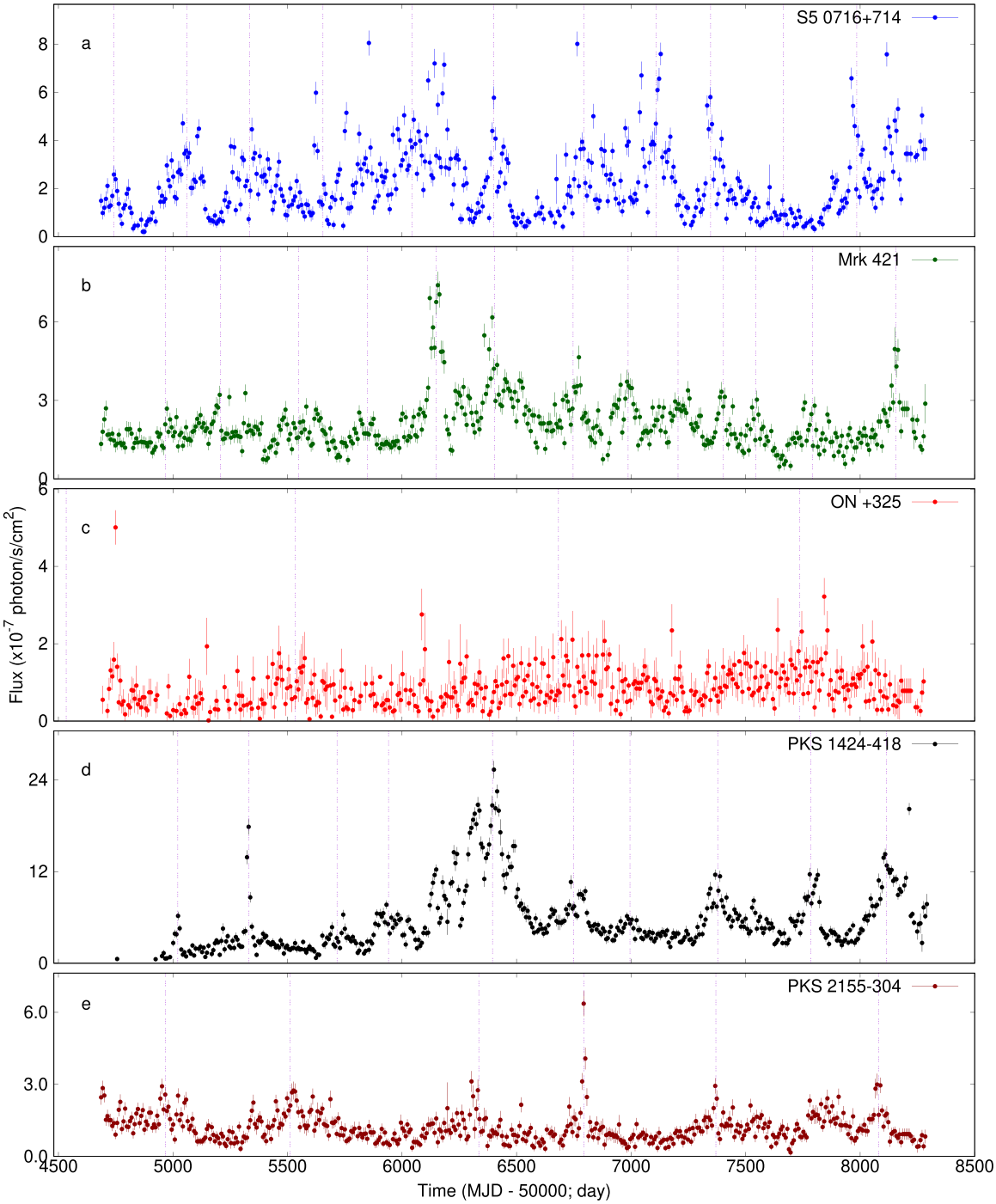

Figure 5. Decade-long *Fermi*/LAT light curves of a blazar displaying quasi-periodic oscillations. The vertical lines mark the tentative position of the peak or centroid of the periodic flux modulation.

4. Discussion

In this section, we present our interpretation and discussion on the results derived from the above analyses in light of the standard model of blazars, i.e., a black-hole-powered central engine and the extended radio jets providing grounds for particle acceleration and energy-dissipation events.

1. γ-ray variability in blazars: In the variability analysis, a quantified measure of the flux modulations as observed in the γ-ray light curves of the blazar sources was provided by computing their fractional variabilities. The numerical values listed in the 7th column of Table 1 suggest that blazar sources are distinctly characterized by their remarkable activity in the γ-ray band. The γ-ray variable emission can be largely ascribed to the events occurring at the kilo-parsec-scale radio jets aligned within $\sim 5^{\circ}$ to the line of sight. These jets are primarily fed with the energy that could be extracted from the fast-spinning Kerr black hole in the presence of the magnetic field at the rotating accretion disk (Blandford & Znajek 1977; Blandford & Payne 1982; Blandford et al. 2019). Shocks traveling down the jet can produce a power-law

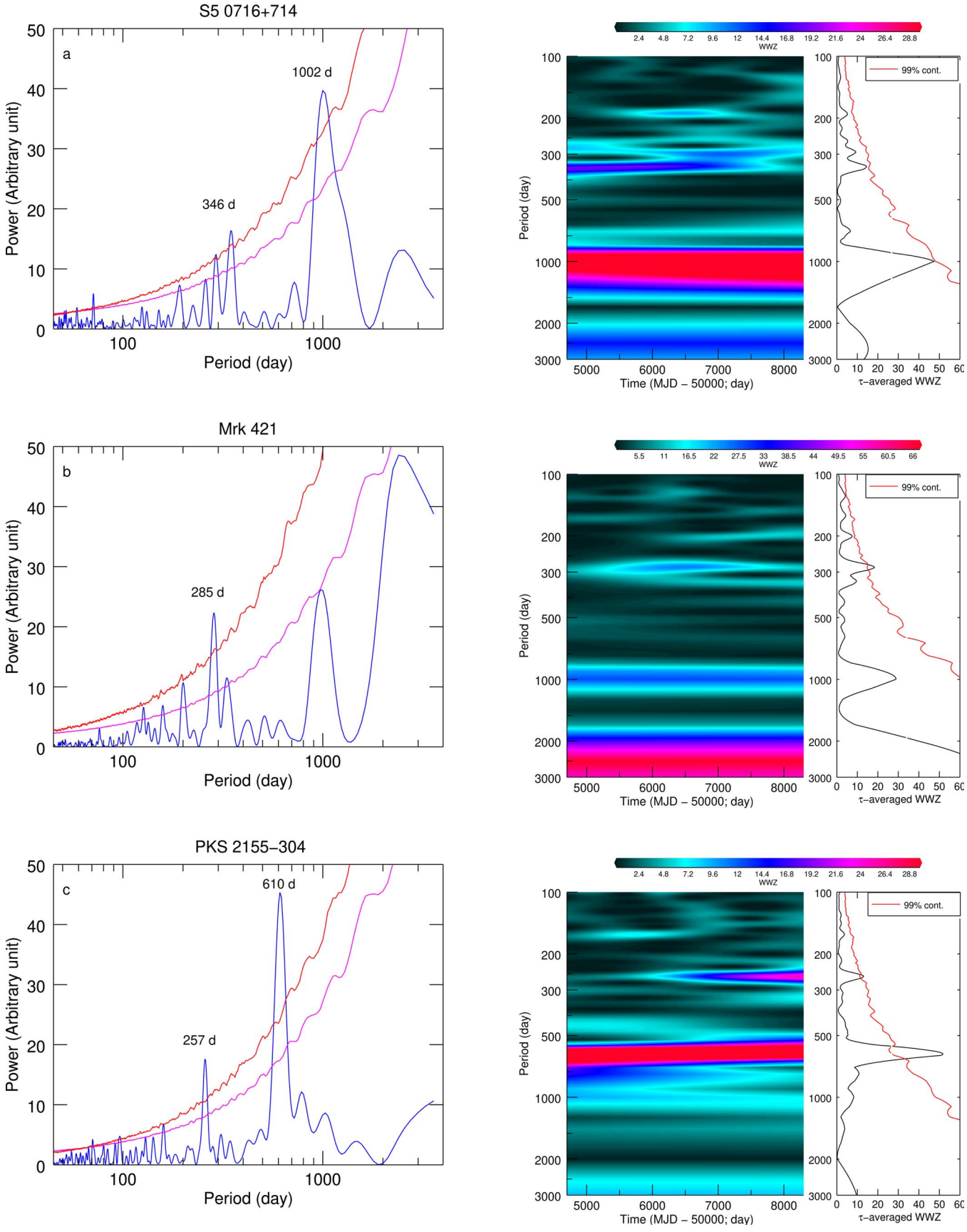

Figure 6. Detection of quasi-periodic oscillations in the γ-ray light curves of blazars. The LS periodograms and 90% and 99% contours are shown by blue, magenta, and red curves, respectively, in the left column panels. The right column panels show the WWZ power with a color gradient, mean WWZ power at a given period as the black curve, and the 99% significance contour as the red curve.

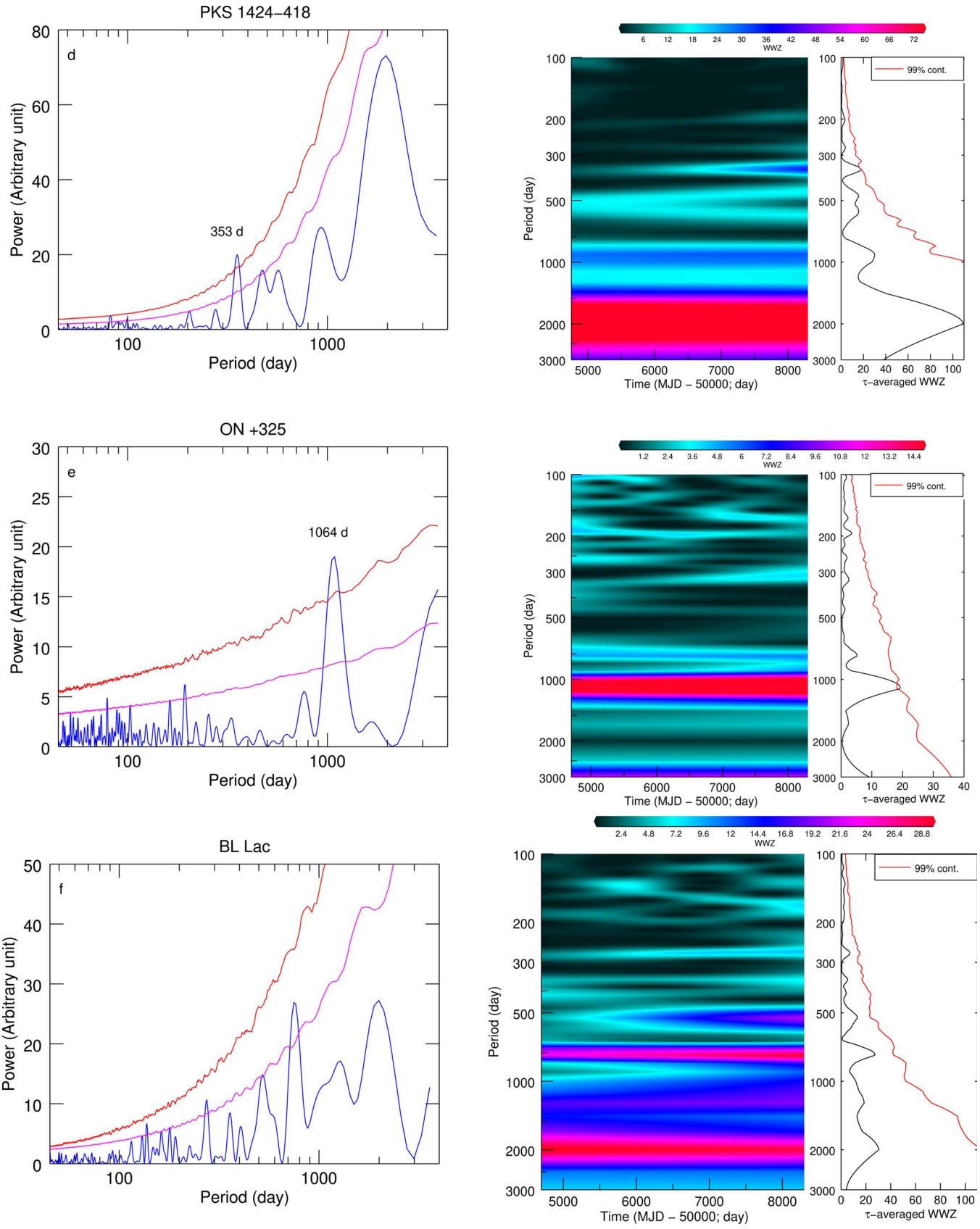

Figure 7. Same as Figure 6, but for different sources.

distribution of energetic electrons $N(\gamma) \propto \gamma^{-p}$ such that the spectral index of the synchrotron emission can be related as $\alpha = (p - 1)/2$. These synchrotron electrons responsible for nonthermal emission might be accelerated to Lorentz factors as high as $\sim 10^6$. Owing to the violent and energetic events prevalent in the jets, individual radio

knots appear to be moving with superluminal motion with apparent velocity up to $\sim 78c$ (Jorstad et al. 2017). Observed γ-ray variability could be intrinsically linked to the combined modulations in a number of components such as the distribution of high-energy particles, seed photons, and the ambient magnetic field at the emission region. On the other hand, it could also be linked to extrinsic (e.g., projection) effects associated with a "plasma blob" that is moving down the jet with bulk Lorentz factors (Γ) as large as ~ 50. In BL Lacs, large Lorentz factors could be conceivable as a viable explanation for the observed high-amplitude variability. In FSRQs, however, this might pose problem because the high-energy emission is most likely produced through inverse-Compton scattering of seed photons external to the jet such that large values of Γ enhance the energy density of these external photons in the comoving frame by $\sim \Gamma^2$. As a result, a pair-production process becomes dominant, which, in turn, should lead to reduced γ-ray emission. But in BL Lacs, due to the lack of circum-nuclear seed photons and SSC being the dominant process producing high-energy emission, the above argument cannot be applied (see Sbarrato et al. 2011). Similarly, nonthermal emission from mini-jets that are further embedded in larger jets can also result in rapid γ-ray variability (Giannios et al. 2009). In hadronic models of blazar emission, γ-ray variability could arise owing to variability in synchrotron emission from extremely high-energy ($E \sim 10^{19}$ eV) protons in highly magnetized (few tens of Gauss) compact regions of the jet with a moderate Doppler factor ~ 15 (Aharonian 2000).

The observed linear correlation between fractional variability and γ-ray spectral index suggests that the sources with a steeper spectrum exhibit greater variability. Theoretically, one might expect such a relation in several cases. For instance, if the emission comes from a smaller volume than the lower-energy emission volume, as in the radiative shock or turbulent extreme multi-zone models, the fluctuations have higher relative amplitudes and shorter timescales. Similarly, the observed flux could be more strongly dependent on the Doppler factor when the spectrum is steeper. In addition, a steeper spectrum indicates that the energies of the emitting particles are close to their upper limits, so that radiative losses are more severe and perhaps their acceleration is more sporadic, causing greater variability. The observed steep slope of the linear fit on the FV-index plane strongly supports the last scenario.

2. Flux distribution: The analysis of the flux distribution of the *Fermi*/LAT light curves of the sample sources suggests that for most of the sources studied in this work, the best-fit PDF closely follows a log-normal distribution. A similar result is obtained by Shah et al. (2018), who used the average monthly *Fermi*/LAT flux for 50 bright blazars. The observed log-normal distribution of the blazar flux has been interpreted in terms of disk processes. Accordingly, the log-normal flux distribution could be indicative of a disk–jet connection in blazars. The fluctuations in the disk, contributing to flux variability, can take place at different radii and, thereby, be dictated by viscosity fluctuations in accordance with the local viscous timescales. In turn, these modulate the mass accretion rates at larger distances from the black hole. Variable emission from accretion disks owing to a variable accretion rate could be driven by uncorrelated fluctuations in the α-parameter taking place at different radii of the disk (see Lyubarskii 1997). The observed log-normal distribution of the blazar flux suggests multiplicative coupling of these perturbations at the disk, as opposed to additive coupling, as in shot-noise-like perturbation (Arévalo & Uttley 2006). If the radiation is relativistically beamed, γ-variability in blazars could arise due to a combination of both source intrinsic events, such as instabilities at the disk and the jet, and source extrinsic geometrical and projection effects. Furthermore, the radiation by the up-scattered photons depends both on the population of the seed photons as well as the high-energy particles that contribute to the up-scattering. In such a scenario, no single variable parameter can be considered as dominant to the variable emission; rather, all possible contributing factors such as the variable magnetic field and high-energy particle density, seed-photon density acted upon by the particle acceleration, and diffusion processes could be coupled in a complex manner resulting in the log-normal distribution of the variable emission from the sources.

On the other hand, a normal flux distribution can be interpreted as integrated emission from individual shock or magnetic-reconnection events occurring stochastically in large-scale turbulent jets (e.g., Bhatta et al. 2013; Xu et al. 2019). It is possible to interpret both kinds of distributions as being special cases of a more general class of skewed distribution, such as Pareto distributions, with variable degrees of skewness. In the context of relativistic jets, such a distribution could be a natural consequence of emission from Poynting flux-dominated jets that hosts mini-jets distributed isotropically within the emission region and that gets ejected close to the line of sight with a high bulk Lorentz factor of ~ 50. In such a scenario, the resulting flux distribution has been found to hold the rms–flux relation (see Biteau & Giebels 2012). Similarly, in the acceleration-due-to-shock scenario, a small perturbation in the acceleration timescale can result in the variability of the particle number density that is a linear combination of Gaussian and log-normal processes. Based on the relative weight associated with these processes, it can, in turn, determine the dominant shape of the flux distribution (see Sinha et al. 2018, and the references therein). If the variability in gamma-ray emission is dictated by such variability in the number density of the accelerated particles, then it is natural for the flux distribution to appear both as Gaussian and log-normal. Such a scenario, where both additive and multiplicative processes operate at varying degrees along the extended jet, also looks plausible.

In blazars, although we infer the variability properties from the jet emission, the primary source of variability could still be associated with fluctuations in the disk processes. These fluctuations could then propagate through the relativistic jets affecting the jet processes and become altered due to the relativistic effects, e.g., flux amplification and time dilation. In blazars, although the disk emission is often completely swamped by the nonthermal emission from the jets, a

careful and detailed study of the flux distribution of blazars should be able to trace the origins of variability back to the disk and thereby constrain the disk–jet connection.

3. Symmetry analysis: We adopted a simple yet novel approach to investigate the blazar emission regions. For this purpose, a statistical analysis studying flux rise and decay in the γ-ray light curves of a sample of sources was performed. The study aimed to unravel an intrinsic difference in the distribution of the flux rise and decay rates, which, if intrinsic to the source, should be associated with two inherently different mechanisms, e.g., particle acceleration and energy dissipative processes, respectively. However, as revealed by the K-S test, we do not observe a significant difference between the rising and decaying profiles of the flux distribution (which we find surprising and counterintuitive, as physical mechanisms driving the flux rise due to particle acceleration mechanisms such as shocks and magnetic reconnection should operate during different timescales from the cooling timescales due to emission processes, mainly considered to be inverse-Compton processes). In this context, it is natural to expect a characteristic difference between the flux rise and decay rates of long-term γ-ray light curves. Nevertheless, these two different processes operating in various timescales could be blended over the extent of the jet such that the overall distribution takes a form that is not easily distinguishable.

   It should be pointed out that the method of symmetry analysis presented in this work differs from the one in which the rise and decay timescales are estimated by fitting exponential curves to well-resolved individual flares as in the works by Meyer et al. (2019), Chatterjee et al. (2012), and Abdo et al. (2010a). In such a case, the asymmetry in the flare could depend upon individual flares. But in the approach adopted in this work, the results rather provide a statistical measure of the average flux-doubling timescales during a wide range of flux changes, which includes both flaring and non-flaring (quiescent) states. This is reflected in the observed wide range of timescales corresponding to the diverse rates with large standard deviations presented as errors in the average timescales (see the sixth column in Table 4). It should be noted that, despite the different approaches to this analysis, the results of this work are in close agreement with those of works that indicate no significant asymmetry between the rise and decay flux profiles. Interestingly, similar results were reported in the studies using long-term optical observation of the sources S5 0716+714 (see Li et al. 2017) and BL Lac (see Guo et al. 2016).

   The timescale estimated using the average flux rise/decay rates (τ) can also shed light onto one of the most important issues yet unresolved in blazar physics, namely, the location of the γ-ray production site in reference to the central black hole. In the literature, we mainly find two compelling arguments on the location of the origin of the γ-ray emission relative to the central engine. Based on the observed rapid (few minutes) γ-ray variability (e.g., see Aharonian et al. 2007; Ackermann et al. 2016), it is argued that the emission should originate at compact regions close to the central black hole ($\sim 20 r_g$), where the bulk of the gravitational potential energy of the infalling matter is released and processed into radiative energy. However, to avoid an eventual depletion of the γ-ray photons due to pair production in a compact region, this requires a large Doppler factor, typically $\delta > 60$ to explain the observed γ-rays. On the other hand, most of the γ-ray flare events have been found to coincide with the ejection of radio knots and the rotation of the polarization angle at the mm-VLBI cores that lie at a distance of few kilo-parsecs (kpc) from the central engine (see, e.g., Jorstad & Marscher 2016; Marscher 2016; Blinov et al. 2018). Also, as γ-ray flaring events are commonly observed to last a few weeks, it can be argued that γ-ray emission is produced at the parsec-scale distance away from the black hole. In such a context, the results obtained from the symmetry analysis can be used to estimate the size of the emission region where γ-ray variability arises and, thereby, obtain a lower limit for the distance between the black hole and the γ-ray emission sites. If we let $r \sim \Gamma^2 \tau c$ for a typical $\Gamma = 15$ with mean $\tau = 22$ days, we obtain $\sim$4 pc. This supports the idea that γ-ray emission could be predominantly produced along the jets on parsec-scale distances, as opposed to regions within a few tens of gravitational radii. To reconcile both of these ideas, it is suggested that the blazar variability as observed in the γ-ray light curves could be a combination of the variable emission originating at both locations, i.e., the low-amplitude fast variability might chiefly originate at the innermost regions—where conversion of gravitational potential energy of infalling matter into high-energy emission is most efficient—and the γ-ray flaring events, flux brightening at least by a factor of a few tens, that last about a few weeks could be located at a distance of a few pc.

4. Power spectral density: We find that the PSDs that best represent the periodogram of γ-ray light curves of the 20 well-known sources are consistent with a single power law of the functional form $P(\nu) \propto \nu^{-\beta}$ where the slope index ranges between 0.8 and 1.5. In the given sample-source light curves, the majority of the slope indexes tend to center around 1.0. Similar results were obtained by Sobolewska et al. (2014) in their PSD analysis of γ-ray light curves of 13 blazars, although their work followed a different method of PSD estimation. This is interesting because $\beta = 1$, often known as the flicker noise, is exactly halfway between random walk ($\beta = 2$) and white noise ($\beta = 0$), and is prevalent in nature (see Press 1978). The flicker noise diverges when integrated from a finite high frequency to lower frequencies—toward zero frequency. But the divergence, being logarithmic, is so slow that the noise maintains its appearance over several orders of frequencies up to arbitrarily low values. Therefore, flicker noises are long-memory processes and therefore can appear coherent over several decades in timescale. For the case of blazars, although our instrument primarily detects Doppler-boosted emission from the jets, it can possess the memory of the events occurring at the accretion disk, especially the disk modulations, such as changes in the accretion rates, viscosity, magnetic field, etc., that could be coupled with the jet processes such that the disk instabilities could drive the jet emission variability. In other words, jet

emission might "remember" disk processes, and this indicates a strong disk–jet connection.

In general, the power-law-type PSD seen in most power spectra of blazar variability can also be explained in the context of a turbulent flow behind a propagating shock (Marscher et al. 1992) or a standing/reconfinement shock in blazar jets (Marscher et al. 2008). If the emission from a single dominant turbulent cell becomes enhanced due to Doppler boosting, it contributes to the temporal frequency corresponding to the size or velocity of the cell. The stochastic nature of turbulence implies that cells of various sizes will be Doppler enhanced over time depending on their velocity and angle to the line of sight. Eventually, this will result in a variability spectrum over a wide range of temporal frequencies that is consistent with the power-law noise seen in blazars (see Wiita 2011). In a similar context, the magnetic field at the accretion disk could be fairly magnetized owing to the material accreted over a considerable period of time. In such an event, the magnetic field can extract the vast rotational energy by threading the black hole and channel into the jet as the bulk power of the relativistic jets. Moreover, as the radiation power is only 10% of the total jet power, a significant contribution to the jet contents could be provided by poynting flux (Ghisellini et al. 2014), which then can facilitate the rampant magnetic-reconnection events triggering stochastic particle acceleration and energy dissipation at various temporal and spatial scales. If the observed variable γ-ray emission is produced in such a scenario, the variability power spectrum should closely resemble a power-law shape.

5. Quasi-periodic oscillations: We found the presence of year-timescale QPOs in some of the sources with a high significance over the power-law PSDs. The detected γ-ray QPOs can potentially offer profound insights on the nature of high-energy emission processes taking place in the sources. In particular, the studies can shed light on a number of current blazar issues such as the disk–jet connection, origin of relativistic jets from the central engine, and other extreme conditions near the fast-rotating supermassive black holes. In principle, the origin of the QPOs can be primarily conceived of in three scenarios: supermassive binary black hole (SMBBH) systems, an accretion disk, and jet instabilities. Some of the possible explanations for the origins of QPOs are discussed below.
   (a) SMBBH system: In the context of an SMBBH system, the observed timescales can be interpreted as the Keplerian periods of the secondary black hole around the central black hole as given by $T = 2\pi a^{3/2}(G\,M)^{-1/2}$ with $M = M_p + M_s \sim 10^9\,M_\odot$, where M_s and M_p are the corresponding masses, respectively, and a is the length of the semimajor axis of the elliptic orbit. Over the long course of merging galaxies, the dynamical friction present in the system can gradually smooth the elliptical orbits into circular orbits. Then, assuming a typical AGN total mass of $M = M_p + M_s \sim 10^9\,M_\odot$ and a mass ratio M_s/M_p in the range 0.1–0.01, the separation between the black holes can be estimated as on the order of a few parsecs. Such a binary systems can undergo orbital decay due to the emission of low-frequency (a few tens of nano-Hertz) gravitational waves (GW), which could be detected by future GW missions. For such a system, the GW-driven orbital decay timescale can be estimated applying

$$\tau_{\rm insp} = 3.05 \times 10^{-6}\left(\frac{M}{10^9\,M_\odot}\right)^{-3}\left(\frac{a}{r_g}\right)^4 \text{ yr}, \quad (8)$$

   (see Peters 1964), a few thousands years, rather short span of time relative to cosmic timescales.
   (b) Accretion disk: Year-timescale periodicity in blazars can be explained in the context of instabilities intrinsic to the accretion disk. To modulate flux periodically, a bright hotspot could be revolving around the central black hole with a Keplerian period, τ_k, given by

$$\tau_k = 0.36\left(\frac{M}{10^9\,M_\odot}\right)^{-1/2}\left(\frac{a}{r_g}\right)^{3/2} \text{ days}, \quad (9)$$

   where a is the length of the semimajor axis of the elliptic orbits. Assuming circular orbits, for a typical black hole of mass of $10^9\,M_\odot$, the radius of the Keplerian orbit for a year timescale can be estimated to be a few tens of gravitational radii (r_g). Similarly, in the case of globally perturbed thick accretion disks, the disk can undergo p-mode oscillations with a fundamental frequency that can be approximated as

$$f_0 \approx 100\left(\frac{r}{r_g}\right)^{-3/2}\left(\frac{M}{10^8\,M\odot}\right)^{-1} \text{ day}^{-1} \quad (10)$$

   (see An et al. 2013, and the references therein).

   To include the effects of a strong gravitational field near a fast-spinning supermassive black hole, the frame dragging effect can warp the inner part of the accretion disk. This might lead to the nodal precession of the tilted plane of the disk better known as the *Lense–Thirring precession*. The period of such a precession can be expressed as

$$\tau_{\rm LT} = 0.18\left(\frac{1}{a_s}\right)\left(\frac{M}{10^9\,M_\odot}\right)\left(\frac{r}{r_g}\right)^3 \text{ days}, \quad (11)$$

   where a_s, M, and r represent the dimensionless spin parameter, mass of the black hole, and the radial distance of the emission region from the black hole, respectively. For a $10^9\,M_\odot$ black hole with a maximal spin ($a_s = 0.9$), a year timescale would correspond to the inner part of the accretion disk extending on the order of a few tens of r_g. In blazars, the precession of the disk can also lead to a jet precession, thereby, resulting in the periodic emission (e.g., Liska et al. 2018).
   (c) Jets: The observed quasi-periodic flux modulations can also be linked to the relativistic motion of the emission regions along the helical path of the magnetized jets (e.g., Camenzind & Krockenberger 1992). In particular, when emission regions move along the helical path of a jet with a large bulk Lorentz factor, Γ, relativistic effects become dominant such that periodic flux modulations can appear due to the periodic changes in the viewing angle. In such a scenario, the rest frame flux ($F'_{\nu'}$) and observed flux

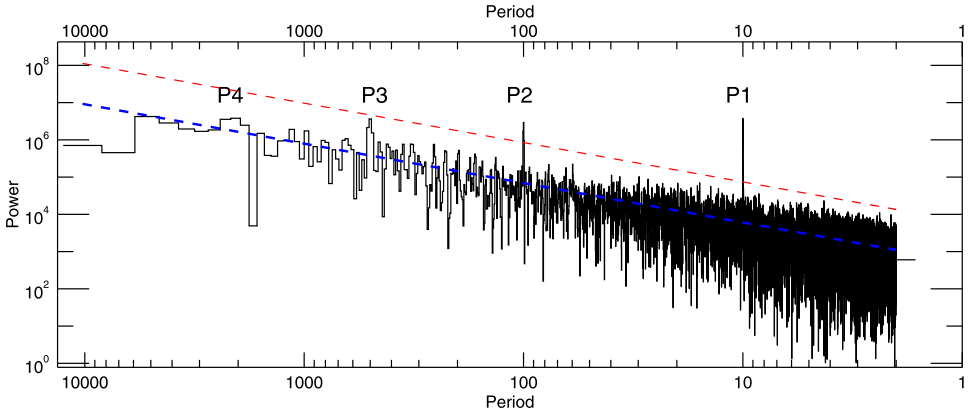

Figure 8. Discrete Fourier periodogram of an evenly spaced light curve simulated by applying a model PSD with a spectral index of 1.5. Sinusoidal waves with periods of 10, 100, 500, and 2000 in arbitrary time units are superimposed on the pure power-law PSD. The blue line represents the log-linear fit to the periodogram, and the red line shows the 99% significance contour.

(F_ν) are related through the relations

$$F_\nu(\nu) = \delta(t)^{3+\alpha} F'_{\nu'}(\nu) \quad \text{and}$$
$$\delta(t) = 1/\Gamma(1 - \beta\cos\theta(t). \tag{12}$$

If we leave the intrinsic flux of the emission region unchanged but change the viewing angle, the corresponding ratio of the observed flux to the intrinsic flux for a given change in the angle $\Delta\theta$ can be expressed as

$$\Delta \log F = -(3 + \alpha)\delta\Gamma\beta \sin\theta\Delta\theta. \tag{13}$$

For illustrative purpose, for blazar emission with a typical γ-ray spectral index ($\alpha = 1.5$) and viewing angles in the 1°–5° range, a slight change in the viewing angle, e.g., $\sim$1°, is sufficient to produce an apparent flux twice as bright (see Bhatta 2018, Figure 4). Similarly, QPOs can originate in blazar jets owing to recurring boosts of turbulent cells behind a propagating shock. If the biggest dominant structure stands out, it will exhibit enhanced Doppler boosting that contributes to the QPO component. However, it is possible that, due to the stochastic nature of turbulence, the cell would gradually decay causing the amplitude of the QPO to diminish accordingly over a period of time (see Wiita 2011).

It should be stressed that the dominance of red noise in blazar light curves often gives rise to a general skepticism toward the actual presence of the QPOs in blazars, particularly QPOs at the low-frequency (LF) ends frequently reported in the literature. Consequently, many authors tend to adopt a conservative measure for the significance, such as $\gtrsim$99.99% over the PSD, required to establish their existence. However, we argue that if we take such a strict approach toward the significance, we could risk overlooking many interesting features in AGNs, and thereby, we may miss exciting physics. To illustrate our point, we present a periodogram of a pure power law of spectral index 1.5 on which purely sinusoidal waves of the periods 10, 100, 500, and 2000 days, but of the same intensity, are superimposed, as shown in Figure 8. The simulated light curve is evenly spaced so that the 99% significance is computed using Equation (16) in Vaughan (2005). The figure shows that for the same amplitude of the periodic modulation, the significance of the peaks gradually decreases as we move from HF to LF such that even in a relatively ideal situation of purely sinusoidal modulations present in the evenly spaced observations, the corresponding spectral peaks can get drowned by the strong power-law trend, which is ever-rising, and can consequently fail to pass the 99% significance test. A similar situation might arise when LF QPOs are unable to maintain phase coherence over more than a few oscillations. In such cases, performing statistical analyses using multiple methods, e.g., carrying out both frequency- and time-based analyses (see Bhatta 2019), would be more useful. Furthermore, a year-scale QPOs could arise in the various scenarios discussed above (see also Ackermann et al. 2015; Bhatta 2017, 2018, 2019). Now, it is a challenging task to break the apparent degeneracy in the models to single out the actual process behind the detection. The task would require an in-depth analysis of multifrequency light curves applying multiple approaches to the time-series analysis.

5. Conclusion

We performed an in-depth time domain analysis of decade-long (2008–2018) *Fermi*/LAT light curves of a sample of 20 bright blazars. We found that γ-ray emission from blazars is highly pronounced and variable over diverse timescales. As one of characteristic features, a steep linear trend was observed in the correlation between the fractional variability and the γ-ray spectral index, suggesting that the variability is highly sensitive to its spectral slope. The γ-ray flux of the blazars is found to be distributed in a way that is closely approximated as a log-normal PDF. Statistical analyses of the flux rising and decay rates in the γ-ray light curves show that both distributions are very similar, and therefore, no significant asymmetry between the flux rising and decay profiles was detected. Moreover, most of the sources appear to exhibit a linear rms–flux relation indicating that higher flux states are often more variable. Furthermore, to constrain the statistical nature of such variability over a wide range of temporal frequencies, extensive MC simulations were performed to estimate the PSDs that best represent the blazar γ-ray periodogram. The study shows that the PSDs are consistent with a single power law, $P(\nu) \propto 1/\nu$, with spectral indexes centered around 1.0, indicating that the nature of the variability as flicker noise, therefore, might be driven by long-memory processes. Additionally, a closer inspection of the Lomb–Scargle and WWZ periodograms of some of the sources in the

sample, including S5 0716+714, Mrk 421, ON +325, PKS 1424−418, and PKS 2155−304, reveal spectral features that signify the presence of year-timescale QPOs that are highly significant over the possible artifacts usually found in blazar light curves.

G.B. acknowledges the financial support by the Narodowe Centrum Nauki (NCN) grant UMO-2017/26/D/ST9/01178. We would like to express our gratitude to Prof. Staszek Zola for kindly allowing us to use their computational facility for this research. We would also like to thank Prof. Michal Ostrowski and Prof. Alan Marscher for fruitful discussions on the γ-ray variability of blazars. The authors are grateful to the anonymous referee for his/her comments that significantly improved the quality of this work.

Facility: *Fermi*/LAT.

Software: HEAsoft, FTOOLS, and fitdistrplus (Delignette-Muller & Dutang 2015).

Appendix A
Decade-long *Fermi*/LAT Light Curves of Blazars

Figures 9 displays the light curves of the blazars studied here.

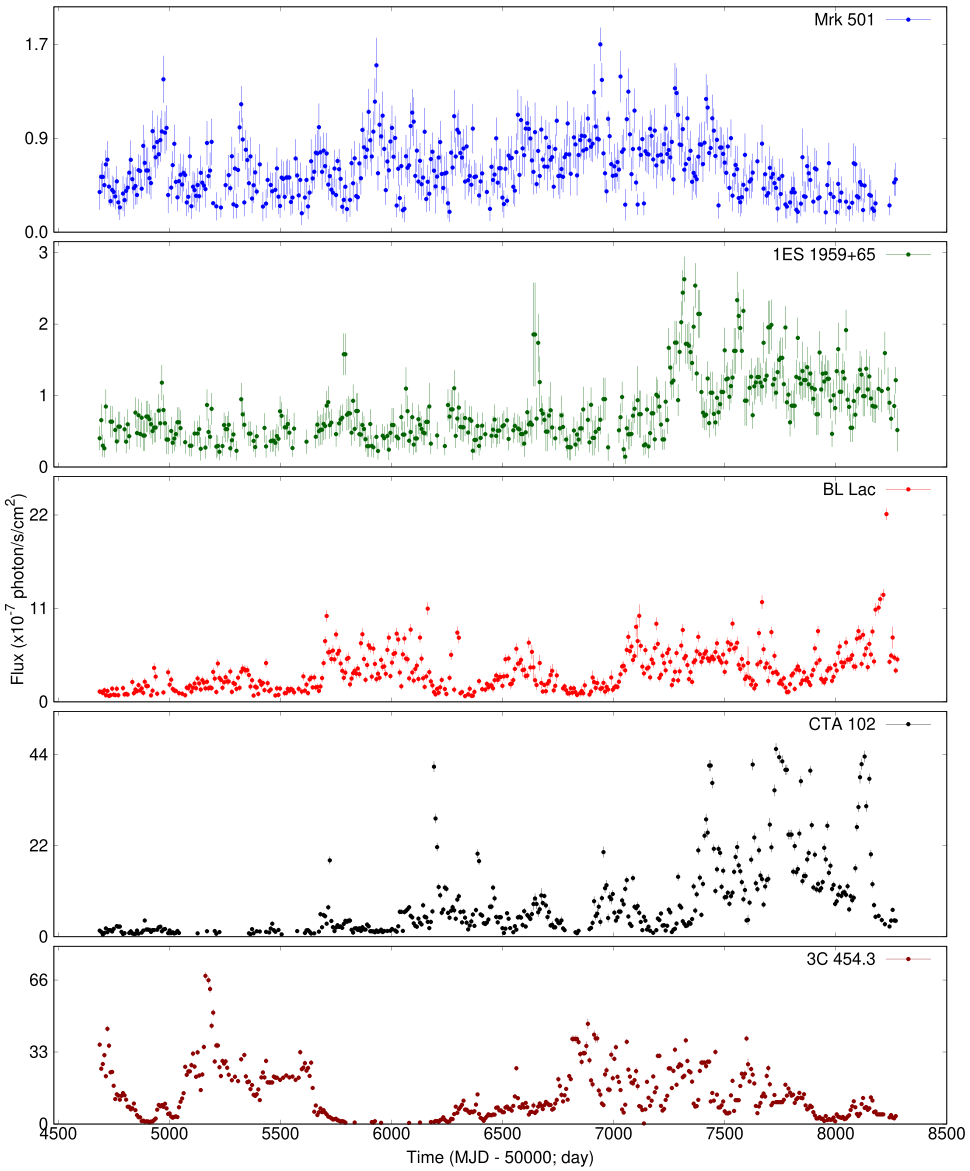

Figure 9. Weekly binned *Fermi*/LAT light curves of the sample blazar listed in Table 1.

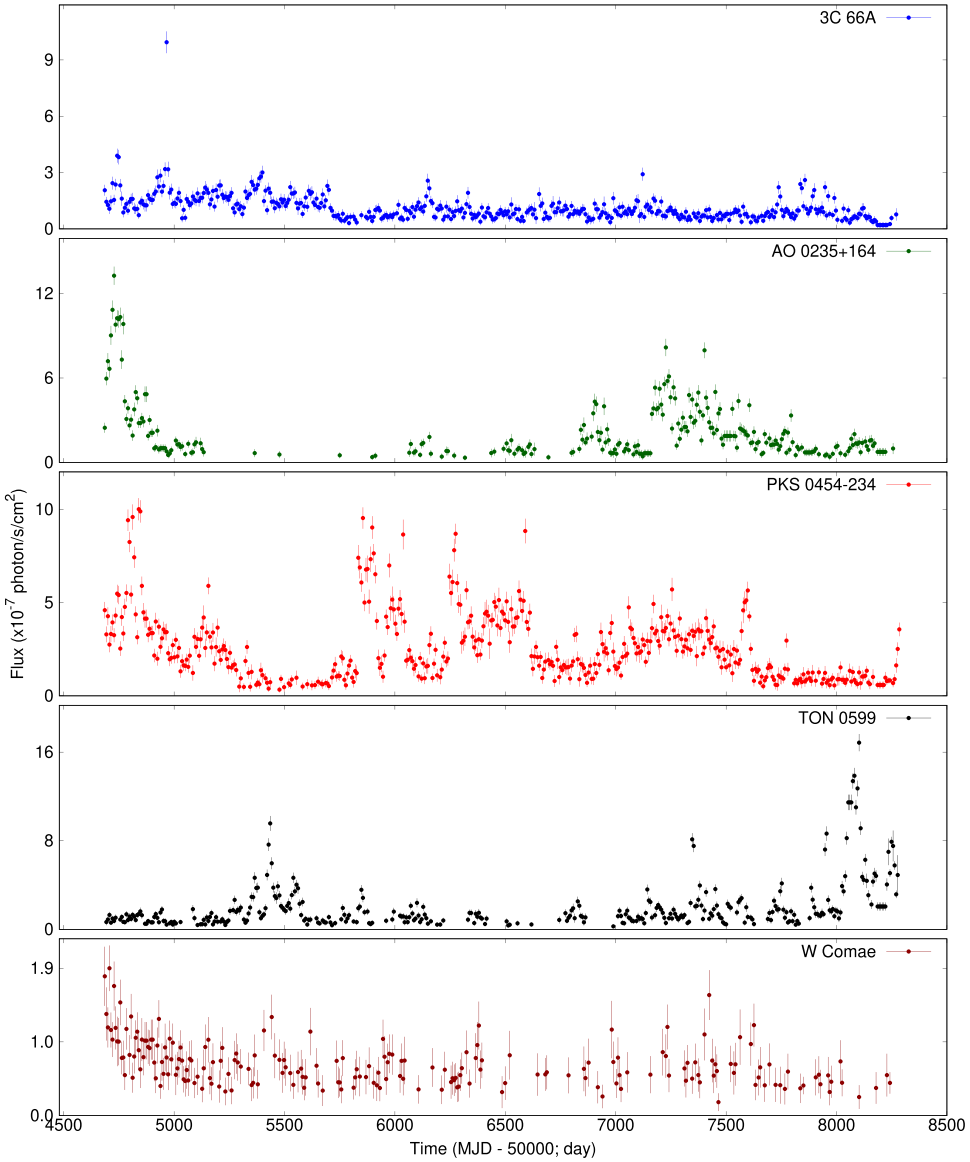

Figure 9. (Continued.)

Appendix B
Fitting of Blazar Flux Distribution Using Weighted Least-squares Method

Table 6 contains the fit statistics for the γ-ray flux distribution of the Fermi/LAT sources.

Table 6
Log-normal and Normal Distribution Fit Statistics for the γ-Ray Flux Distribution of the *Fermi*/LAT Sources Using Weighted Least-squares Method

	Log-normal Fit			Normal Fit		
Source Name (8)	m (9)	s (10)	χ^2/dof (11)	μ (12)	σ (13)	χ^2/dof (14)
3C 66A	-0.03 ± 0.02	0.52 ± 0.02	4.19/6	0.81 ± 0.07	0.75 ± 0.07	24.58/6
AO 0235+164	0.34 ± 0.08	0.90 ± 0.09	7.63/10	-24.37 ± 2.07	6.73 ± 0.53	11.66/10
PKS 0454−234	0.72 ± 0.04	0.75 ± 0.03	17.04/17	0.82 ± 0.51	2.54 ± 0.27	15.21/17
S5 0716+714	0.63 ± 0.04	0.72 ± 0.03	20.02/16	1.63 ± 0.14	1.63 ± 0.12	34.72/16
Mrk 421	0.62 ± 0.02	0.35 ± 0.01	36.22/16	1.94 ± 0.04	0.71 ± 0.03	56.54/16
TON 0599	0.25 ± 0.07	0.79 ± 0.09	19.27/12	-19.07 ± 1.42	5.33 ± 0.36	27.05/12
ON +325	-0.32 ± 0.03	0.62 ± 0.03	25.45/9	0.78 ± 0.03	0.48 ± 0.03	23.88/9
W Comae	-0.51 ± 0.03	0.40 ± 0.02	11.25/10	0.61 ± 0.02	0.21 ± 0.02	41.99/10
4C +21.35	0.83 ± 0.09	1.11 ± 0.10	13.12/13	-47.73 ± 3.67	12.97 ± 0.93	23.43/13
3C 273	0.84 ± 0.04	0.70 ± 0.06	25.98/12	-34.07 ± 2.64	9.52 ± 0.65	39.21/12
3C 279	1.30 ± 0.04	0.87 ± 0.06	39.84/16	-63.96 ± 4.19	17.56 ± 1.06	57.24/16
PKS 1424−418	1.52 ± 0.03	0.66 ± 0.02	8.54/15	4.16 ± 0.26	3.51 ± 0.52	73.60/15
PKS 1502+106	1.08 ± 0.05	0.85 ± 0.05	8.26/10	-51.32 ± 5.73	14.17 ± 0.99	13.33/10
4C +38.41	0.64 ± 0.07	1.01 ± 0.07	24.30/13	-37.57 ± 2.98	10.25 ± 0.75	38.12/13
Mrk 501	-0.63 ± 0.02	0.45 ± 0.02	20.36/15	0.54 ± 0.02	0.27 ± 0.01	15.55/15
1ES 1959+65	-0.39 ± 0.03	0.53 ± 0.02	29.06/15	0.71 ± 0.03	0.35 ± 0.03	98.54/15
PKS 2155−304	0.09 ± 0.02	0.48 ± 0.02	16.45/9	1.10 ± 0.03	0.48 ± 0.03	42.73/9
BL Lac	1.03 ± 0.04	0.71 ± 0.03	35.63/17	1.05 ± 0.69	3.41 ± 0.32	23.65/17
CTA 102	1.49 ± 0.09	1.22 ± 0.11	18.90/15	-97.12 ± 11.90	26.18 ± 2.98	40.00/15
3C 454.3	2.34 ± 0.06	1.00 ± 0.05	52.79/12	-33.57 ± 28.02	27.80 ± 7.17	46.30/12

Note. For the normal fit, μ and σ are presented in units of flux in $10^{-7} \times$ counts s^{-1} cm^{-2}, whereas for the log-normal fit, m is in units of the natural log of flux.

Appendix C
Probability Density Function for Blazar Flux Distribution

Figure 10 displays the probably density function for the blazar flux distribution.

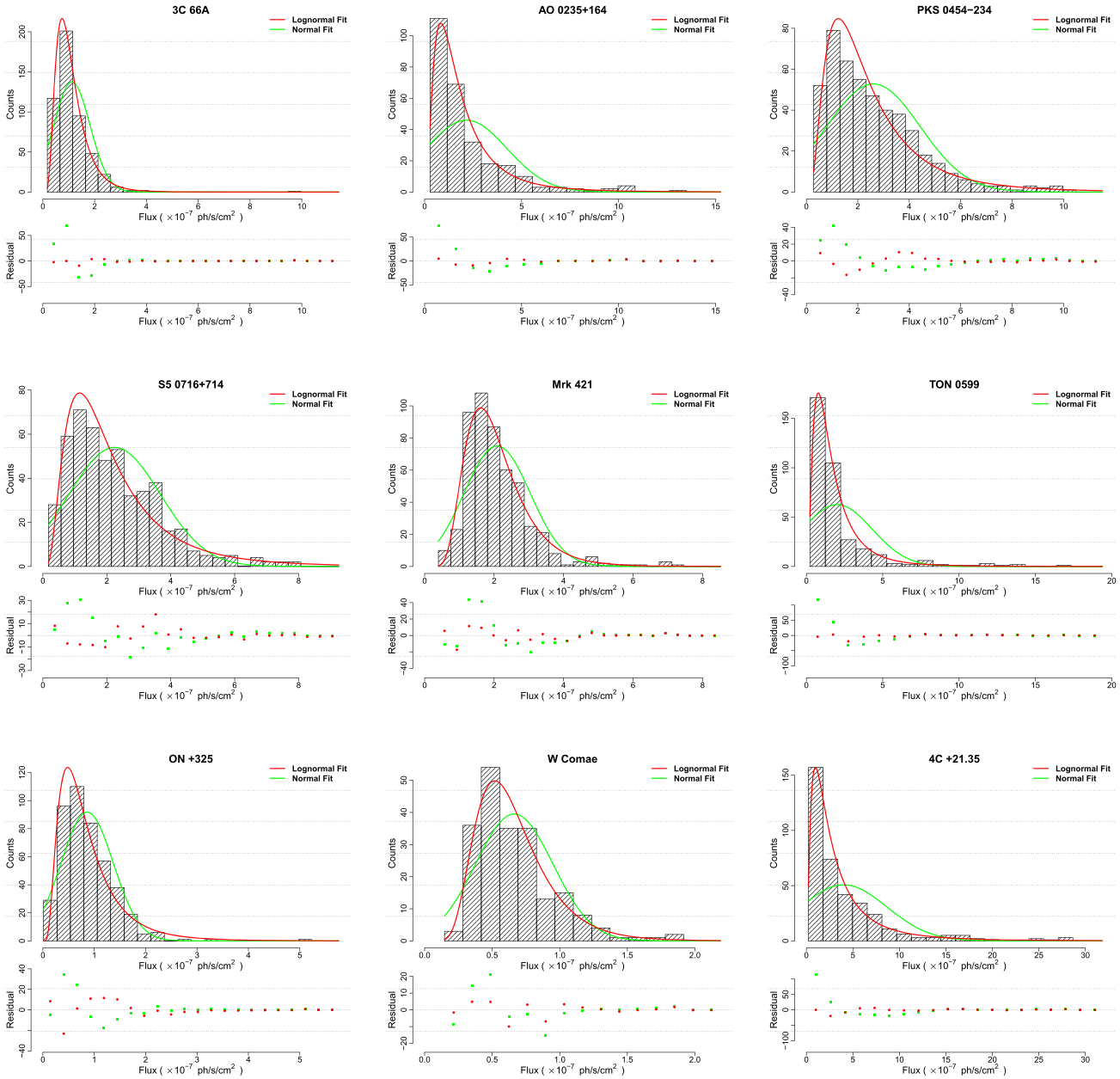

Figure 10. Log-normal and normal distribution fits to the γ-ray flux distributions of the *Fermi*/LAT sources listed in Table 1 using the MLE method.

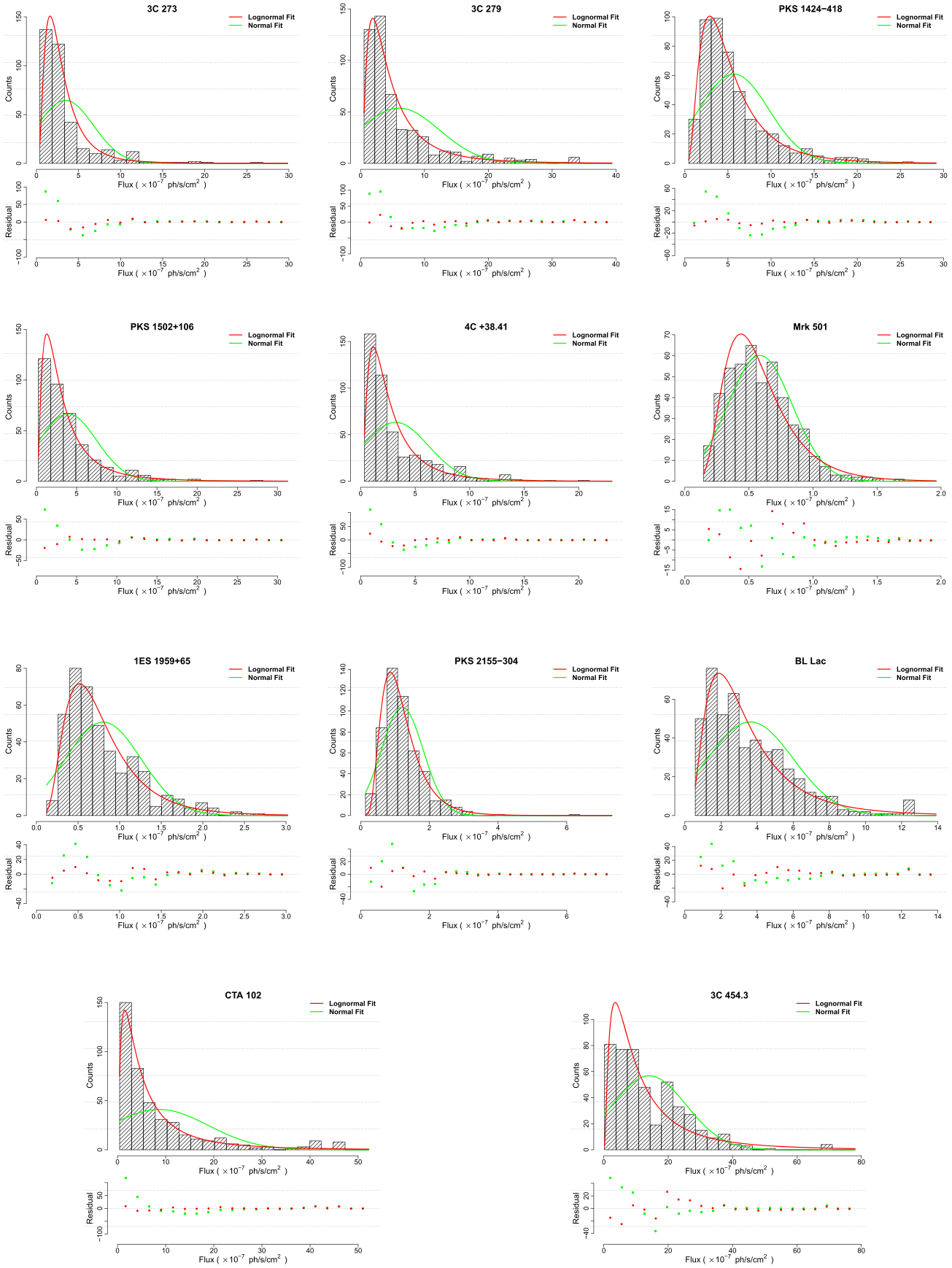

Figure 10. (Continued.)

Appendix D
Rms–Flux Relation in Blazar

Figure 11 illustrates the blazar rms-flux relation.

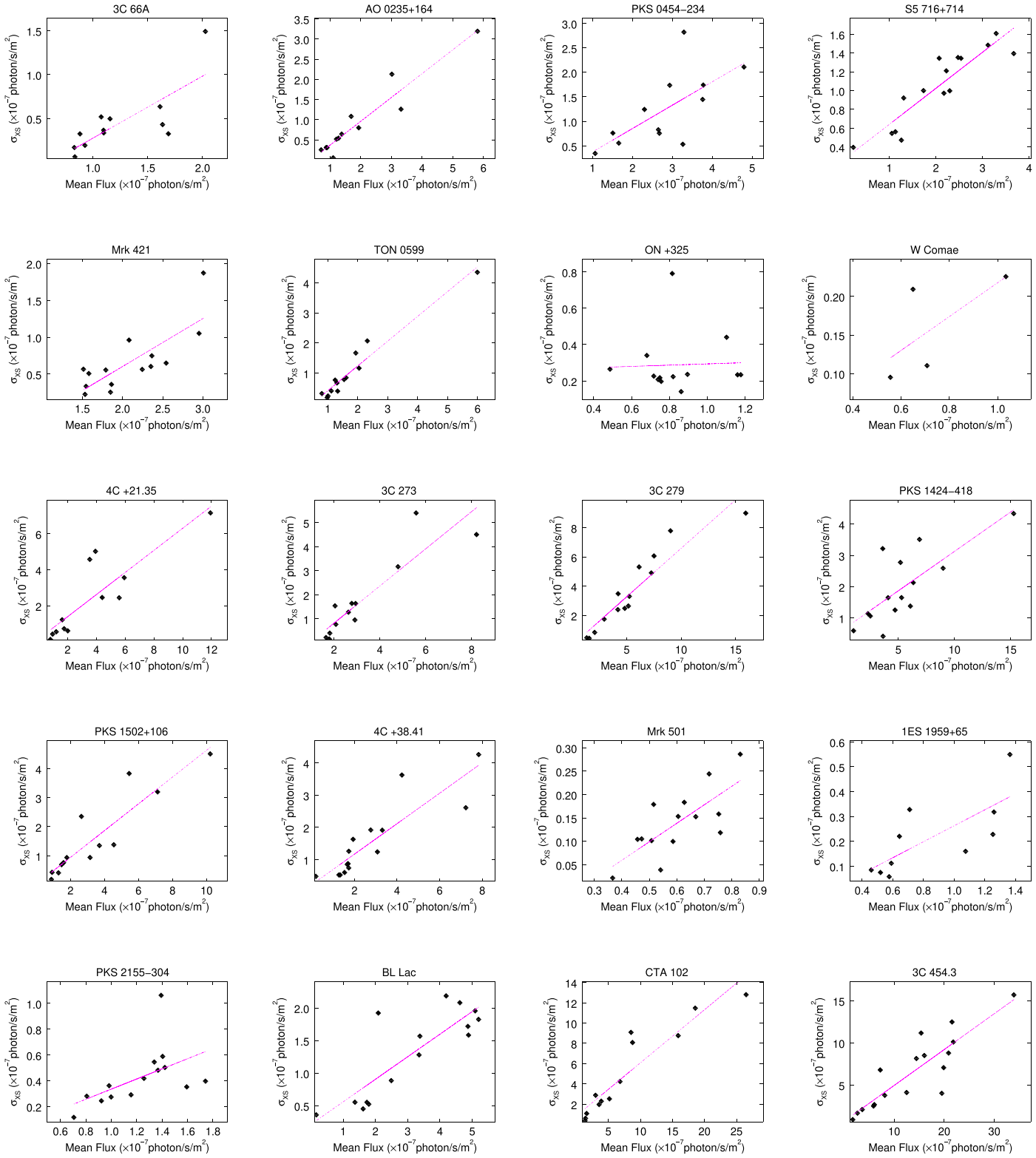

Figure 11. Rms–Flux relation in the gamma-ray light curves of the sample blazars. The magenta line represents the linear fit to the observations.

Appendix E
Power Spectral Density of Blazar

Figure 12 displays the blazar power spectral densities.

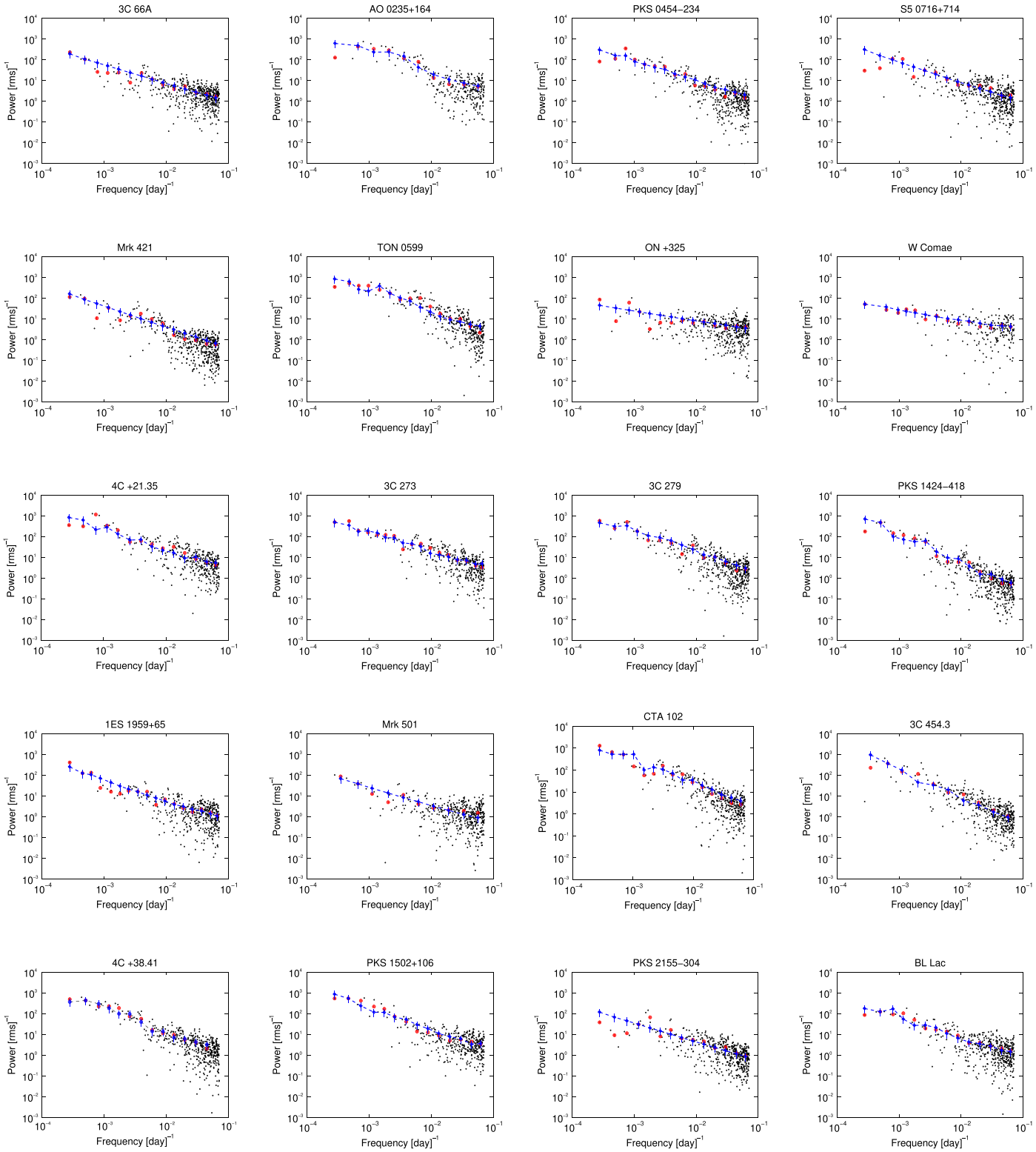

Figure 12. Power spectral density of the gamma-ray light curves of the blazars. Discrete Fourier periodogram (black), binned periodogram (red), and the best-fit PSD (blue).

ORCID iDs

Gopal Bhatta https://orcid.org/0000-0002-0705-6619

References

Abdo, A. A., Ackermann, M., Ajello, M., et al. 2010a, ApJ, 722, 520
Abdo, A. A., Ackermann, M., Ajello, M., et al. 2010b, ApJS, 188, 405
Acero, F., Ackermann, M., Ajello, M., et al. 2015, ApJS, 218, 23
Ackermann, M., Ajello, M., Albert, A., et al. 2015, ApJL, 813, L41
Ackermann, M., Anantua, R., Asano, K., et al. 2016, ApJL, 824, L20
Aharonian, F., Akhperjanian, A. G., Bazer-Bachi, A. R., et al. 2007, ApJL, 664, L71
Aharonian, F. A. 2000, NewA, 5, 377
Ait Benkhali, F., Hofmann, W., Rieger, F. M., et al. 2020, A&A, 634, A120
An, T., Baan, W. A., Wang, J.-Y., Wang, Y., & Hong, X.-Y. 2013, MNRAS, 434, 3487
Arévalo, P., & Uttley, P. 2006, MNRAS, 367, 801
Atwood, W. B., Abdo, A. A., Ackermann, M., et al. 2009, ApJ, 697, 1071
Bell, M. E., Tzioumis, T., Uttley, P., et al. 2011, MNRAS, 411, 402
Benitez, E., Cabrera, J. I., Fraija, N., et al. 2015, arXiv:1512.01219
Bhatta, G. 2017, ApJ, 847, 7
Bhatta, G. 2018, Galax, 6, 136
Bhatta, G., Goyal, A., Ostrowski, M., et al. 2015, ApJL, 809, L27
Bhatta, G., Stawarz, Ł., Markowitz, A., et al. 2018, ApJ, 866, 132
Bhatta, G., Stawarz, Ł., Ostrowski, M., et al. 2016a, ApJ, 831, 92
Bhatta, G., & Webb, J. 2018, Galax, 6, 2
Bhatta, G., Zola, S., Stawarz, Ł., et al. 2016b, ApJ, 832, 47
Bhatta, G., Webb, J. R., Hollingsworth, H., et al. 2013, A&A, 558A, 92B
Bhatta, G. 2019, MNRAS, 487, 3990
Biteau, J., & Giebels, B. 2012, A&A, 548, A123
Błażejowski, M., Sikora, M., Moderski, R., & Madejski, G. M. 2000, ApJ, 545, 107
Blandford, R., Meier, D., & Readhead, A. 2019, ARA&A, 57, 467
Blandford, R. D., & Payne, D. G. 1982, MNRAS, 199, 883
Blandford, R. D., & Znajek, R. L. 1977, MNRAS, 179, 433
Blinov, D., Pavlidou, V., Papadakis, I., et al. 2018, MNRAS, 474, 1296
Böttcher, M. 2019, Galax, 7, 20
Camenzind, M., & Krockenberger, M. 1992, A&A, 255, 59
Chatterjee, R., Bailyn, C. D., Bonning, E. W., et al. 2012, ApJ, 749, 191
Chevalier, J., Sanchez, D. A., Serpico, P. D., et al. 2019, MNRAS, 484, 749
Czerny, B. 2006, in ASP Conf. Ser. 360 AGN Variability from X-Rays to Radio Waves, ed. C. M. Gaskell et al. (San Francisco, CA: ASP), 265
Delignette-Muller, M. L., & Dutang, C. 2015, Journal of Statistical Software, 64, 4
Dermer, C. D., & Schlickeiser, R. 1993, ApJ, 416, 458
Event Horizon Telescope Collaboration, Akiyama, K., Alberdi, A., et al. 2019, ApJL, 875, L6
Fan, J. H., Lin, R. G., Xie, G. Z., et al. 2002, A&A, 381, 1
Fan, J. H., Yang, J. H., Liu, Y., et al. 2016, ApJS, 226, 20
Fossati, G., Maraschi, L., Celotti, A., Comastri, A., & Ghisellini, G. 1998, MNRAS, 299, 433
Foster, G. 1996, AJ, 112, 1709
Ghisellini, G., Celotti, A., Fossati, G., et al. 1998, MNRAS, 301, 451
Ghisellini, G., Righi, C., Costamante, L., & Tavecchio, F. 2017, MNRAS, 469, 255
Ghisellini, G., Tavecchio, F., Foschini, L., & Ghirlanda, G. 2011, MNRAS, 414, 2674
Ghisellini, G., Tavecchio, F., Maraschi, L., et al. 2014, Natur, 515, 376
Giannios, D., Uzdensky, D. A., & Begelman, M. C. 2009, MNRAS, 395, L29
Guo, Y. C., Hu, S. M., Li, Y. T., et al. 2016, MNRAS, 460, 1790
Gupta, A. 2018, Galax, 6, 1
IceCube Collaboration, Aartsen, M. G., Ackermann, M., et al. 2018a, Sci, 361, eaat1378
IceCube Collaboration, Aartsen, M. G., Ackermann, M., et al. 2018b, Sci, 361, 147
Isobe, N., Sato, R., Ueda, Y., et al. 2015, ApJ, 798, 27
Jorstad, S., & Marscher, A. 2016, Galax, 4, 47
Jorstad, S. G., Marscher, A. P., Morozova, D. A., et al. 2017, ApJ, 846, 98
Kushwaha, P., Sinha, A., Misra, R., et al. 2017, ApJ, 849, 138
Li, H. Z., Jiang, Y. G., Guo, D. F., et al. 2016, PASP, 128, 074101
Li, Y. T., Hu, S. M., Jiang, Y. G., et al. 2017, PASP, 129, 14101
Liska, M., Hesp, C., Tchekhovskoy, A., et al. 2018, MNRAS, 474, L81
Lomb, N. R. 1976, Ap&SS, 39, 447
Lyubarskii, Y. E. 1997, MNRAS, 292, 679
Madejski, G. (Greg), & Sikora, M. 2016, ARA&A, 54, 725
Maraschi, L., Ghisellini, G., & Celotti, A. 1992, ApJL, 397, L5
Marscher, A. 2016, Galax, 4, 37
Marscher, A. P. 2014, ApJ, 780, 87
Marscher, A. P., Gear, W. K., & Travis, J. P. 1992, in Variability of Blazars, ed. E. Valtaoja & M. Valtonen (Cambridge: Cambridge Univ. Press), 85
Marscher, A. P., Jorstad, S. G., D'Arcangelo, F. D., et al. 2008, Natur, 452, 966
Mastichiadis, A., & Kirk, J. G. 2002, PASA, 19, 138
Mattox, J. R., Bertsch, D. L., Chiang, J., et al. 1996, ApJ, 461, 396
McKinney, J. C., Tchekhovskoy, A., & Blandford, R. D. 2012, MNRAS, 423, 3083
Meyer, M., Scargle, J. D., & Blandford, R. D. 2019, ApJ, 877, 39
Nakagawa, K., & Mori, M. 2013, ApJ, 773, 177
Narayan, R., Igumenshchev, I. V., & Abramowicz, M. A. 2003, PASJ, 55 L69
Papadakis, I. E., & Lawrence, A. 1993, MNRAS, 261, 612
Peters, P. C. 1964, PhRv, 136, 1224
Press, W. H. 1978, ComAp, 7, 103
Prokhorov, D. A., & Moraghan, A. 2017, MNRAS, 471, 3036
Raiteri, C. M., Villata, M., Tosti, G., et al. 2003, A&A, 402, 151
Rieger, F. 2019, Galax, 7, 28
Sandrinelli, A., Covino, S., Dotti, M., & Treves, A. 2016, AJ, 151, 54
Sandrinelli, A., Covino, S., & Treves, A. 2014, ApJL, 793, L1
Sandrinelli, A., Covino, S., Treves, A., et al. 2017, A&A, 600, A132
Sbarrato, T., Foschini, L., Ghisellini, G., et al. 2011, AdSpR, 48, 998
Scargle, J. D. 1982, ApJ, 263, 835
Shah, Z., Mankuzhiyil, N., Sinha, A., et al. 2018, RAA, 18, 141
Sikora, M. 1994, ApJS, 90, 923
Sikora, M., & Begelman, M. C. 2013, ApJL, 764, L24
Sillanpää, A., Haarala, S., Valtonen, M. J., Sundelius, B., & Byrd, G. G. 1988, ApJ, 325, 628
Sinha, A., Khatoon, R., Misra, R., et al. 2018, MNRAS, 480, L116
Sobolewska, M. A., Siemiginowska, A., Kelly, B. C., & Nalewajko, K. 2014, ApJ, 786, 143
The Fermi-LAT collaboration 2019, arXiv:1902.10045
Timmer, J., & Koenig, M. 1995, A& A, 300, 707
Uttley, P., McHardy, I. M., & Papadakis, I. E. 2002, MNRAS, 332, 231
VanderPlas, J. T. 2018, ApJS, 236, 16
Vaughan, S. 2005, A&A, 431, 391
Vaughan, S., Edelson, R., Warwick, R. S., & Uttley, P. 2003, MNRAS, 345, 1271
Wagner, S. J., & Witzel, A. 1995, ARA&A, 33, 163
Wiita, P. J. 2011, JApA, 32, 147
Xu, J., Hu, S., Webb, J. R., et al. 2019, ApJ, 884, 92
Zhang, B.-K., Zhao, X.-Y., Wang, C.-X., et al. 2014, RAA, 14, 933
Zhang, P.-f., Yan, D.-h., Liao, N.-h., & Wang, J.-c. 2017a, ApJ, 835, 260
Zhang, P.-f., Yan, D.-h., Liao, N.-h., et al. 2017b, ApJ, 842, 10
Zhang, P.-F., Yan, D.-H., Zhou, J.-N., et al. 2017c, ApJ, 845, 82
Zhou, J., Wang, Z., Chen, L., et al. 2018, NatCo, 9, 4599